FISEVIER

Contents lists available at ScienceDirect

Palaeogeography, Palaeoclimatology, Palaeoecology

journal homepage: www.elsevier.com/locate/palaeo



Continuous simulations over the last 40 million years with a coupled Antarctic ice sheet-sediment model



David Pollard^{a,*}, Robert M. DeConto^b

- ^a Earth and Environmental Systems Institute, Pennsylvania State University, University Park, PA, 16802, USA
- ^b Department of Geosciences, University of Massachusetts, Amherst, MA, 01003, USA

ARTICLE INFO

Keywords:
Cenozoic
Bedrock topography
Bedrock erosion
Marine sediments
Antarctic ice sheet evolution

ABSTRACT

Much of the knowledge of Antarctic Ice Sheet variations since its inception \sim 34 Ma derives from marine sediments on the continental shelf, deposited in glacimarine or sub-ice environments by advancing and retreating grounded ice, and observed today by seismic profiling and coring. Here we apply a 3-D coupled ice sheet and sediment model from 40 Ma to the present, with the goal of directly linking ice-sheet variations with the sediment record. The ice-sheet model uses vertically averaged ice dynamics and parameterized grounding-line flux. The sediment model includes quarrying of bedrock, sub-ice transport, and marine deposition. Atmospheric and oceanic forcing are determined by uniform shifts to modern climatology in proportion to records of atmospheric CO_2 , deep-sea-core $\delta^{18}O$, and orbital insolation variations. The model is run continuously over the last 40 Myr at coarse resolution (80 or 160 km), modeling post-Eocene ice, landscape evolution and off-shore sediment packages in a single self-consistent simulation. Strata and unconformities are tracked by recording times of deposition within the model sediment stacks, which can be compared directly with observed seismic profiles. The initial bedrock topography is initialized to 34 Ma geologic reconstructions, or an iterative procedure is used that yields independent estimates of paleo bedrock topography. Preliminary results are compared with recognized Cenozoic ice-sheet variations, modern sediment distributions and seismic profiles, and modern and paleo bedrock topographies.

1. Introduction

A number of studies have considered the whole post-Eocene evolution of the Antarctic Ice Sheet since its main inception $\sim\!34\,\text{Ma}$ at the Eocene-Oligocene boundary (Barrett et al., 1996; Miller et al., 2005; Cramer et al., 2009, 2011; Gasson et al., 2012; Mudelsee et al., 2014; van de Wal et al., 2011; de Boer et al., 2010, 2012; McKay et al., 2016; Stap et al., 2017). These studies attempt to integrate major ice-sheet transitions and variations with long-term records of deep-sea $\delta^{18}\text{O}$ and temperature, atmospheric CO₂ and sea level, and/or 1-D flowline ice-sheet modeling. The individual features considered, with sample data and modeling references, include:

- Sudden inception of continental-scale ice cover at the Eocene-Oligocene boundary ~34 Ma (e.g., Galeotti et al., 2016; DeConto and Pollard, 2003);
- Orbital and longer-period variations in the Oligocene and Miocene (e.g., Palike et al., 2006; Liebrand et al., 2011; De Vleeschouwer et al., 2017), and a gradual transition from terrestrial to marine ice

in West Antarctica due to interior bedrock lowering and subsequent retrograde continental shelf slopes (e.g., Gasson et al., 2016; Levy et al., 2016; Bart et al., 2016; Colleoni et al., 2018a,b),

- Temporary cooling and ice expansion at the Oligocene-Miocene boundary (Mi1 event, Wilson et al., 2008),
- Mid-Miocene climatic optimum and subsequent transition to cooling and ice expansion, ~17 to ~13 Ma (MMCO, MMCT, e.g., Foster and Rohling, 2013; Greenop et al., 2014),
- Pliocene warm period intervals with ice retreat ~3 Ma (e.g., Dowsett et al., 2016; de Boer et al., 2015; Pollard et al., 2015; Golledge et al., 2017),
- Orbitally paced and Northern Hemispherically influenced glacialinterglacial cycles since ~2 Ma with occasional West Antarctic ice collapses in the Pliocene and Pleistocene (e.g., Naish et al., 2009; Pollard and DeConto, 2009).

These studies have focused on links between atmospheric and oceanic climate variations, and their effects on and feedbacks with the ice sheet. Other important elements are long-term variations of bedrock

E-mail address: pollard@essc.psu.edu (D. Pollard).

^{*} Corresponding author.

topography, such as significantly higher subaerial topography in West Antarctica around ~34 Ma and subsequent lowering due to tectonics and erosion (Wilson and Luyendyk, 2009; Wilson et al., 2012, 2013; Bart et al., 2016; Gasson et al., 2016; Stap et al., 2016; Colleoni et al., 2018b), and long-term landscape evolution due to erosion beneath the East Antarctic ice sheet affecting the ice-bed interface (Jamieson et al., 2010, 2014; Sugden and Jamieson, 2018; Paxman et al., 2019a,b). Other aspects such as regional tectonic dynamic topography have generally not been considered (Austermann et al., 2015).

Marine sediments on Antarctic continental shelves, derived from interior continental erosion, transport and deposition under flowing ice, offer a wealth of indirect information on Antarctic ice sheet variations since its inception ~34 Ma. Overall sediment extents and volumes around Antarctica are reasonably well known, along with many seismic profiles supported by cores providing transects of dated layers and major unconformities over the mid to late Cenozoic (reviewed for instance in Cooper et al., 1993; Anderson, 1999; Colleoni et al., 2018a,b; Antarctic Seismic Data Library System SDLS, http://sdls.ogs.trieste.it/). These have not been considered in detail in most of the long-term evolution studies mentioned above, with some exceptions such as Barrett et al. (1996), and total sediment volumes in Wilson and Luyendyk (2009); Wilson et al., (2012).

If coupled ice-sheet and sediment models can simulate these deposits explicitly over long time and space scales, that would enable direct comparisons with the sediment record and help to link it to Cenozoic ice and climate history. A few studies have approached this for Antarctica with erosion and sediment models more or less coupled to ice-sheet models (ten Brink and Schneider, 1995; ten Brink et al., 1995; Bougamont and Tulaczyk, 2003; Pollard and DeConto, 2003, 2007; Golledge et al., 2013; Brinkerhoff et al., 2017), but mostly in 1-D flowline mode and/or over relatively short time periods, not suitable for comparisons with the longer-term Antarctic sediment record. Other coupled studies of ice and erosion on different time and space scales include Oerlemans (1984) and Herman et al. (2018).

In this paper a coupled 3-D continental ice-sheet and sediment model is run continuously from 40 Ma to the present, capturing the Eocene-Oligocene transition and post-Eocene Antarctic evolution and off-shore sediment packages in a single self-consistent simulation. Atmospheric and oceanic forcing is provided by uniform shifts from modern climatology in proportion to records of atmospheric CO_2 , deep-sea-core $\delta^{18}O$, and orbital insolation variations. The sediment model includes quarrying of bedrock, sub-ice transport and deposition, with times of deposition tracked to enable model "strata" and unconformities to be compared with seismic profiles. Initial ice-free bedrock topography is either prescribed from the 34 Ma reconstruction of Wilson et al. (2012), or is determined in an iterative procedure described below. Long-term rates of tectonic thermal subsidence in West Antarctica, and uplift in Marie Byrd Land, are prescribed as in Wilson et al. (2012).

This model-based approach, explicitly integrating processes forward in time, is complementary to the technique of geologic reconstructions that restore modern sediment backwards in time to its original locations (e.g., Wilson et al., 2012). In a companion paper, Paxman et al. (2019b) extend the latter approach to reconstruct maps of bedrock elevations at selected times through the late Cenozoic that can be compared directly with our results, providing insights into the strengths and uncertainties of both studies. Preliminary comparisons between the two studies are described below and in the Supplementary Material.

In order to make the long simulations in this paper feasible, the model resolution is very coarse, 80–160 km. Even though the ice model's use of local parameterizations for grounding-line flux and other fine-scale processes yields results that are not seriously degraded compared to finer resolutions in shorter experiments (Pollard and DeConto, 2012a; Pollard et al., 2015), the coarse resolution can induce model-dependent inaccuracies especially in Height-Mass Balance Feedback (van den Berg et al., 2006; Gasson et al., 2016). Also, there

are major uncertainties in sediment dynamics (weakly non-linear vs. plastic) and in modes of sediment transport (englacial vs. deformation) (Evans et al., 2006; Hildes et al., 2004; Melanson et al., 2013; Meyer et al., 2018).

Despite these uncertainties we suggest that the simulations are worthwhile, if only (i) to demonstrate that ~40 Myr 3-D continental ice sheet-sediment simulations are computationally feasible (~4 days wall-clock time with 80 km resolution), and (ii) to identify individual components needing further improvement. Although preliminary, the resulting 3-D modern marine sediment map can be compared directly with the extensive body of published sediment data including seismic profiles, and the ice-sheet evolution can be assessed critically with the major events in the bulleted list above. Basic model-data comparisons for the current simulations below show encouraging first-order agreement, but with several important misfits. These misfits can help to guide future model improvements, notably in sediment physics, resolution, and climate forcing. The long-term goal is to directly connect Antarctic ice-sheet history with marine sediments, and to provide a framework for relating individual seismic profiles around Antarctica.

Section 2 describes the models and climate forcing. Results are then shown in sections 3 to 5 for a single representative simulation over the last 40 Myr, initialized to the 34 Ma bedrock reconstruction of Wilson et al. (2012). Section 3 briefly describes the model's Cenozoic evolution and compares with observed trends and events, section 4 describes modern sediment distributions simulated by the model, and section 5 shows selected cross-sections of modeled strata comparable to observed seismic profiles. Sections 6 and 7 describe another simulation using an iterative procedure involving multiple 40 Myr runs, which in principle produces model-generated paleo bedrock topographic maps independent of geologically based reconstructions. Conclusions are summarized in section 8. The Supplementary Material contains further details of the climate forcing, various model sensitivity tests, and a summary of comparisons with the companion paper (Paxman et al., 2019b).

2. Models

2.1. Ice sheet model

The ice sheet model (PSUICE-3D, Pollard and DeConto, 2012a) has been applied previously to Antarctica, and validated against past and modern conditions (Pollard and DeConto, 2009, 2012b; Pollard et al., 2016). It uses vertically integrated SIA-SSA ice dynamics, and migrating grounding lines and floating ice shelves with parameterized groundingline flux (Schoof, 2007). Hydrofracture due to surface melt and structural failure of tall ice cliffs are included here (Pollard et al., 2015; DeConto and Pollard et al., 2016). Internal ice temperatures are simulated, with basal sliding and sediment deformation occurring only where the base is at or near the melt point, and no explicit basal hydrology. A Weertman-type basal sliding law over bedrock is used with sliding velocity proportional to the square of basal shear stress, and spatially dependent coefficients as described below.

The model uses a polar stereographic grid centered on the South Pole, with coarse resolution to make 40 Myr-long simulations feasible. The previous coarsest resolution used for the model (40 km, Pollard and DeConto, 2009) would be infeasible for these runs. Here a resolution of 80 km is used for the main run presented below, and 160 km is used for the later iterative simulation. As mentioned above, intrinsically fine-scale processes (sub-grid grounding-line location and flux, and ice cliff failure) are parameterized and do not rely on being resolved explicitly by the model grid, which makes results in short tests quite independent of resolution (Pollard et al., 2015). The time step in all coarse-resolution runs here is 8 years, and one (single-processor) run over 40 Myr takes \sim 4 days at 80 km and \sim 1 day at 160 km.

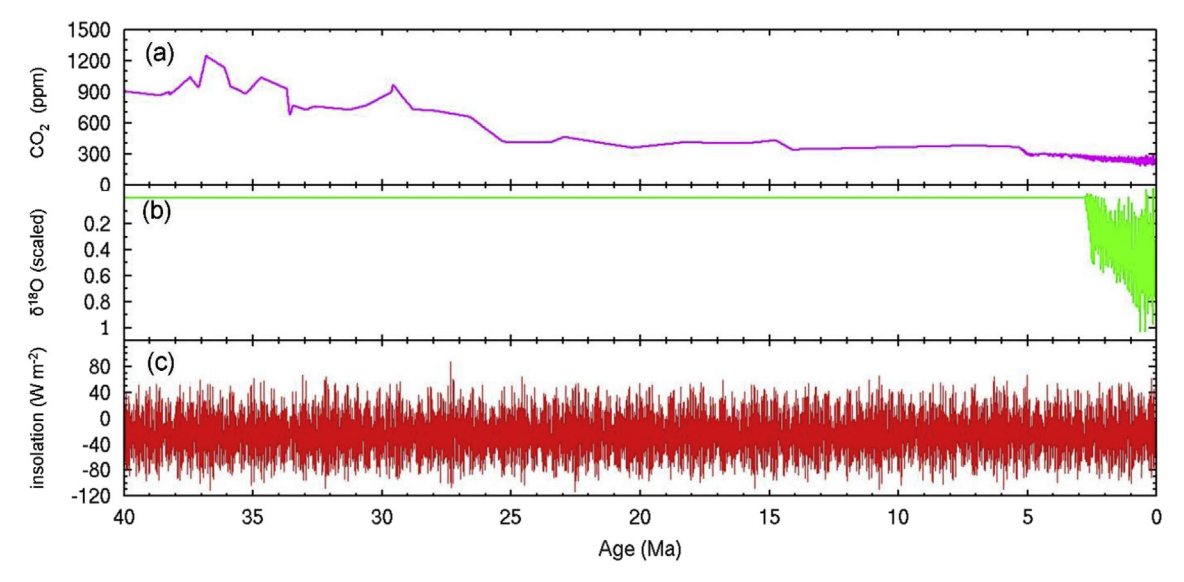


Fig. 1. Forcing time series used to drive the ice-sheet model through the last 40 Myr. (a) Atmospheric CO₂, ppmv: Zhang et al. (2013) before 5 Ma; scaled to deep-seacore δ^{18} O (Lisiecki and Raymo, 2005) after 5 Ma, with 280 ppmv at modern, 180 ppmv at last glacial maximum. (b) Deep-sea-core δ^{18} O, scaled to 0 at modern, 1 at last glacial maximum (Lisiecki and Raymo, 2005), and set to 0 before 2.8 Ma. (c) January mean insolation departure from modern at 80°S, W m⁻² (Laskar et al., 2004).

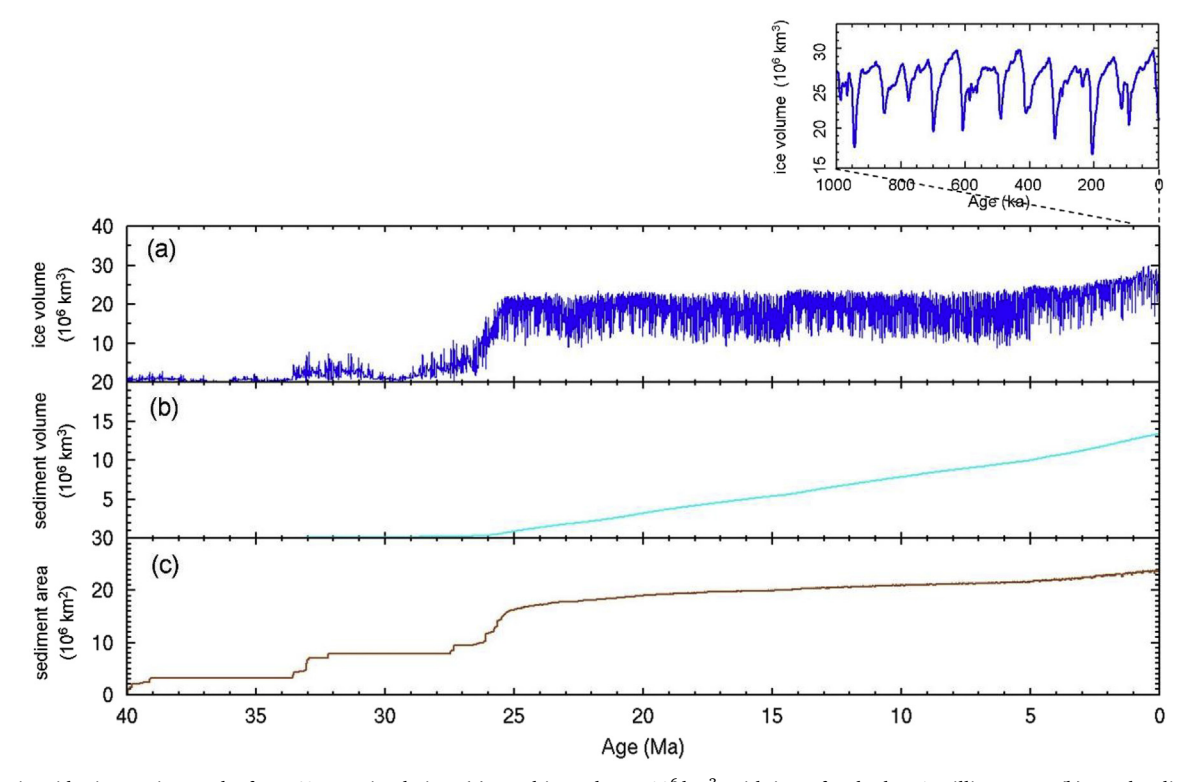


Fig. 2. Domain-wide time-series results for a 40 Myr simulation. (a) Total ice volume, $10^6 \, \mathrm{km}^3$, with inset for the last 1 million years. (b) Total sediment volume, $10^6 \, \mathrm{km}^3$. (c) Total sediment area, $10^6 \, \mathrm{km}^2$.

2.2. Sediment model

The sediment model (Pollard and DeConto, 2007) has been used previously for North America (Clark and Pollard, 1998) and Antarctica (Pollard and DeConto, 2003, 2007). Sediment is generated by erosion of exposed bedrock due to the action of basal ice. The model sediment lies above bedrock, and below the ice if any. Once an appreciable thickness of sediment is generated, it is transported horizontally by the shear force of the overriding ice, which deforms the upper few 10's of centimeters to ~ meter of sediment in the direction of basal ice flow

according to an assumed weakly non-linear sediment rheology. The sediment model involves three main equations: the erosion rate of exposed bedrock (Eq. (1) below), the sediment velocity profile for a given basal shear stress, and the rate of change of sediment thickness due to convergence or divergence of the transport plus local generation by erosion (Pollard and DeConto, 2007). Sediment is deposited (thickens) where the sediment advection converges (mainly at the outer edge of grounded ice), or is removed (thins) where advection diverges. Sediment temperature profiles are also simulated as part of the ice-sediment-bed vertical-column heat diffusion. The upper sediment speed is

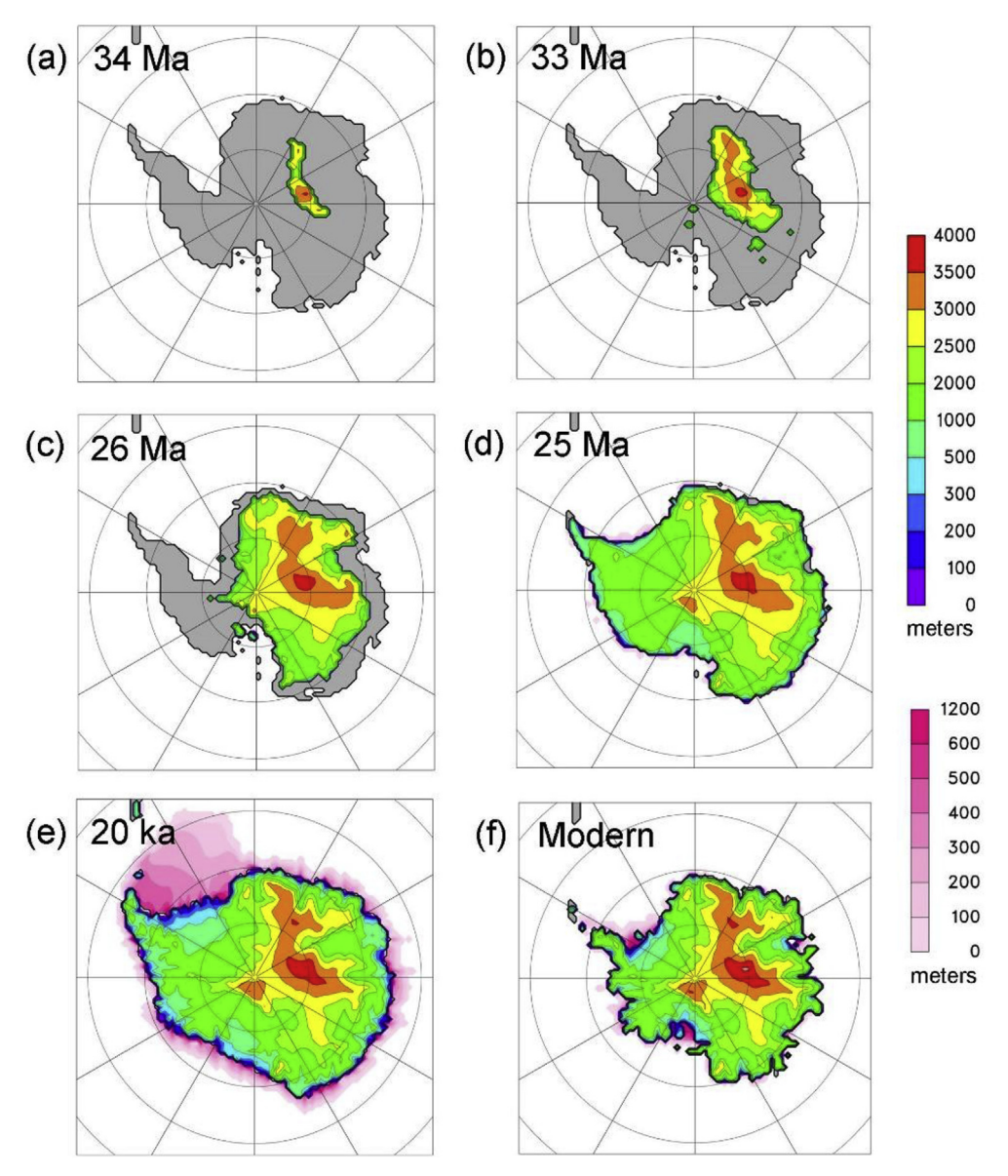


Fig. 3. Ice distributions at selected times during a 40 Myr simulation. Rainbow scale: grounded ice elevation (meters). Pink scale: floating ice thickness (meters). Grey: bare land. (For interpretation of the references to color in this figure legend, the reader is referred to the Web version of this article.)

imparted to the ice, effectively making the bed more slippery where sediment exists.

New sediment (till) is generated by erosion of bedrock where sediment cover does not already exist or is patchy, so that bedrock is exposed to the overlying ice. The fractional exposure increases from 0 to 100% as the grid cell-mean sediment thickness decreases from 0.5 to 0 m. In the exposed fraction, bedrock is eroded at a rate proportional to the work done by ice:

$$E = k \tau_b \nu_b \tag{1}$$

where E is the rate of new sediment generation (m y-1), τ_b is basal ice shear stress on the exposed bedrock (Pa), and v_b is basal ice velocity (m y-1). The quarrying coefficient k is constant in time with typical values 10^{-11} to 10^{-10} m y-1 per (Pa m y-1). Rates of erosion in reality are strongly influenced by bedrock properties such as hardness or roughness, and spatial variations in these properties are represented primarily by basin-by-basin adjustments to k in iterative experiments described later, and to a lesser extent by spatial variations in the bedrock sliding coefficient C via τ_b and v_b in Eq. (2) as described below. Sediment deformation and v_b can be non-zero only where basal

temperatures are at or near the pressure melt point (Pollard and DeConto, 2012a); this is similar to but less explicit than the dependence on basal melt rates in Jamieson et al. (2008, 2010). Note that the term "quarrying" is used in this paper for sub-glacial erosion by any means such as plucking or abrasion, and does not denote a particular mechanism. Any subsequent compaction of buried sediment layers is neglected. Alternate parameterizations of the bedrock erosion rate are described in the Supplementary Material.

Beneath floating ice or open ocean, sediment is not in contact with ice, but can be moved by ocean turbidity currents (Luchi et al., 2018) or by bottom-water currents (Uenzelmann-Neben and Gohl, 2012). This is included crudely in the model by instantaneous "slumping" of oceanic sediment to maintain a maximum surface slope of .0075 (m m⁻¹); an alternate scheme is described in the Supplementary Material. Any pelagic deposition of sediments in areas of open ocean is neglected. At all grid points, times of sediment deposition or removal are recorded, i.e., times when the sediment thickness passes up or down through incremental 10-m values, which enables mapping of 3-D model sediment "strata" that can be compared with observed seismic profiles.

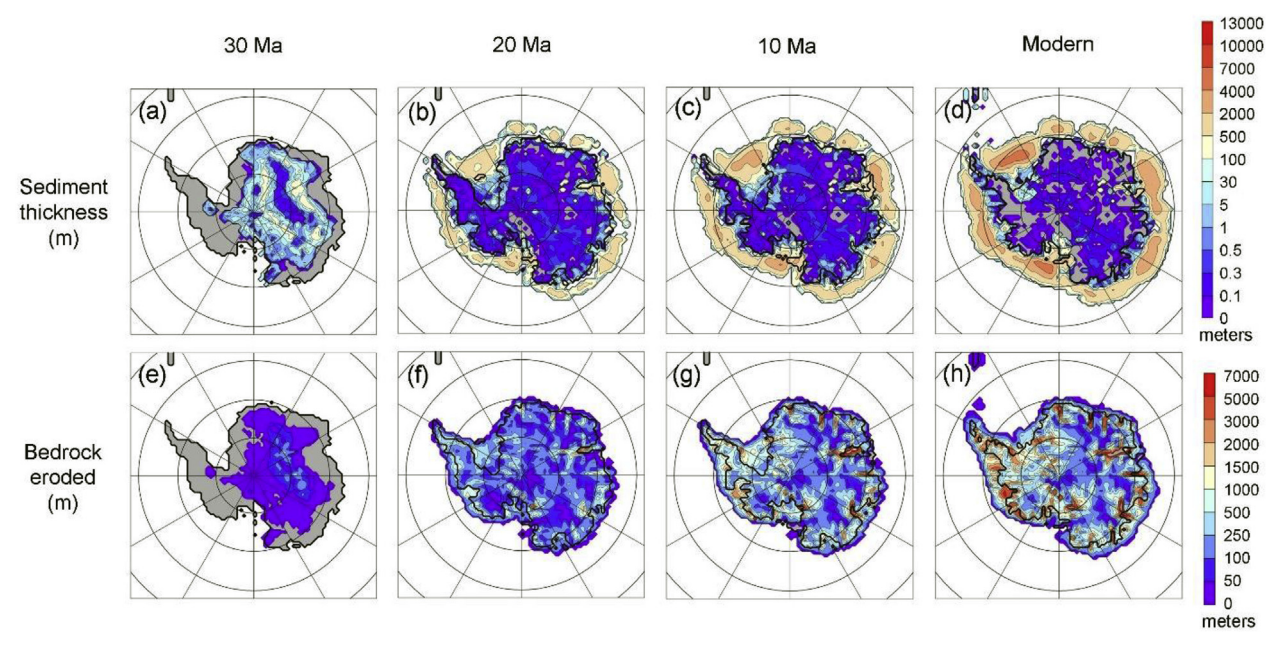


Fig. 4. (a)–(d): Sediment thickness (meters) at selected times during a 40 Myr simulation. (e) to (h), Bedrock erosion depth (meters of eroded bedrock) since the start of the run, multiplied by the ratio of bedrock to sediment densities (ρ_b/ρ_s) , at the selected times.

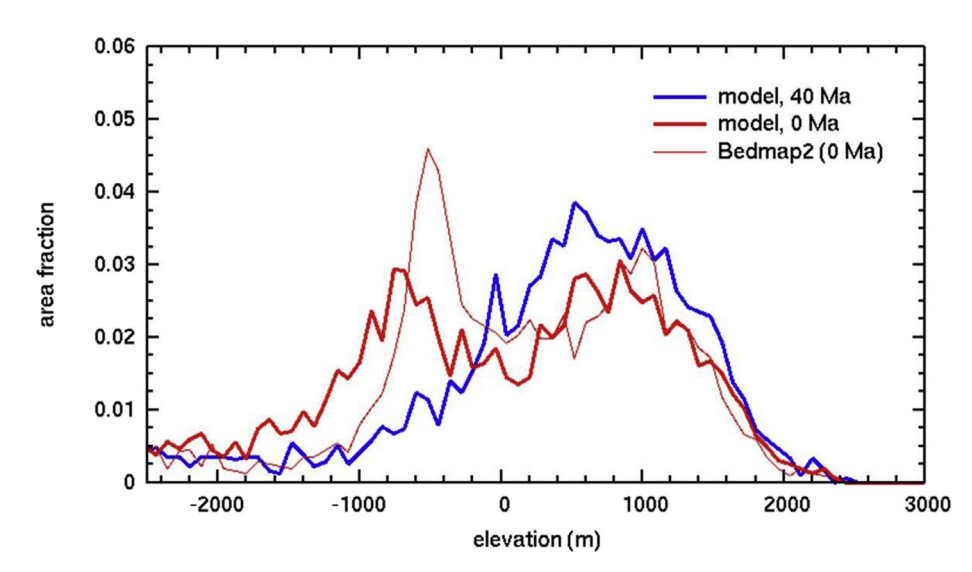


Fig. 5. Hypsometries of bedrock (including sediment) elevations, after local isostatic rebound with all ice removed, for the domain poleward of 65 °S and with bed elevations > -4000 m. Blue curve: Wilson et al. (2012) average of minimum and maximum 34 Ma reconstructions, prescribed at the start of the simulation at 40 Ma. Thick red curve: Model at end of a 40 Myr simulation (modern). Thin red curve: Observed modern (Bedmap2, Fretwell et al., 2013) aggregated to the model grid. The x-axis elevations (meters) are relative to modern sea level, and the y axis is fraction of area per 80-m elevation bin. (For interpretation of the references to color in this figure legend, the reader is referred to the Web version of this article.)

2.3. Bedrock model

Bedrock deformation below the ice load is represented by local isostatic relaxation beneath an elastic lithospheric layer (a standard ELRA model). The isostatic relaxation e-folding time is 3000 years, and the lithospheric flexural rigidity is $10^{25}\,\mathrm{N\,m}$ in East Antarctica and $10^{24}\,\mathrm{N\,m}$ in West Antarctica (Pollard and DeConto, 2012a). All model runs are initialized with no ice and no sediment at 40 Ma, so that all subsequent sediment is model-generated and glacial in origin, and rests on the 40 Ma bedrock surface or the surface eroded into that bedrock.

The rate of bedrock erosion corresponding to Eq. (1) is (ρ_s/ρ_b) E, where $\rho_s = 2050 \, \text{kg m}^{-3}$ is the bulk sedment density and $\rho_b = 2550 \, \text{kg m}^{-3}$ is the density of upper bedrock (based on Wilson et al., 2012). This erosion lowers the model's bedrock surface elevation. Removal of bedrock (with density ρ_b) is partially compensated by uplift due to isostatic relaxation within the denser mantle (with density $\rho_m = 3370 \, \text{kg m}^{-3}$), like bed changes due to ice and ocean loading in the ELRA bedrock model. Consequently, bedrock erosion also lowers the equilibrium bedrock elevation used in the ELRA calculations (h_b^{eq} in Eq.

33 of Pollard and DeConto, 2012a), at a rate (ρ_s/ρ_b) E $(1 - \rho_b/\rho_m)$.

The initial bedrock topography at 40 Ma can be set to the Wilson et al. (2012) reconstruction at the Eocene-Oligocene boundary ~34 Ma. Here we use the simple average of their "minimum" and "maximum" reconstructions; results using the two reconstructions individually are shown in the Supplementary Material. Alternatively, an iterative procedure can be used to determine the initial topography, described later in sections 6 and 7. Gradual long-term tectonic thermal subsidence in West Antarctica, and uplift in Marie Byrd Land, are imposed as in Wilson et al. (2012, their Figs. S2 and S5 respectively), with uniform rates from 34 Ma to the present and none before 34 Ma. As in their study, the West Antarctic subsidence is applied in all experiments, but the Marie Byrd Land uplift is only applied in experiments with their minimum reconstruction, and at 50% in those with their average reconstruction.

An important quantity for the bedrock is the basal sliding coefficient *C* for the ice dynamics, in the power sliding law:

$$v_b = C \tau_b^2 \tag{2}$$

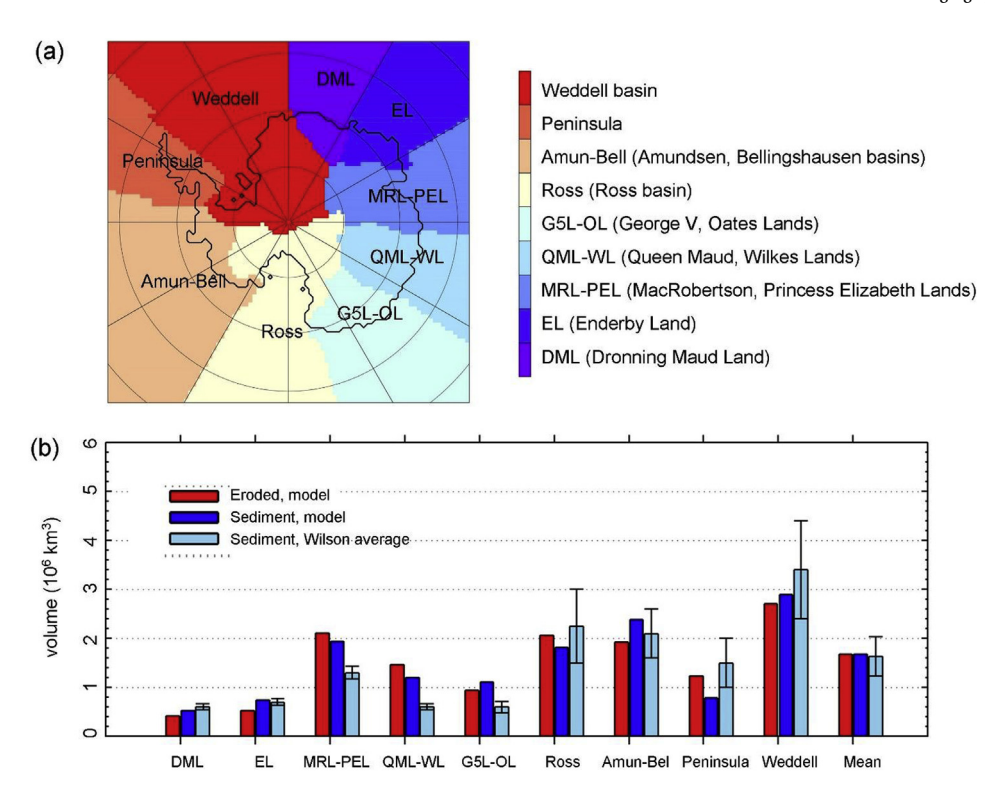


Fig. 6. (a) Sectors used to compare model vs. observed sediment totals, as in Wilson et al. (2012) similar to their Fig. 4. Interior drainage basins are linked with simple longitudinal offshore sectors. Labels match those in Wilson et al. (2012), (b) Total eroded-bedrock and sediment volumes (106 km3) in each sector at the end of a 40 Myr simulation. Red: model bedrock eroded ("quarried") by basal ice, times the ratio of bedrock to sediment densities (ρ_b/ρ_s) . Blue: model sediment. Light blue: observed modern sediment volumes, average of Wilson et al. (2012) minimum and maximum estimates with whiskers showing minimum and maximum. The right-hand set of bars labelled "Mean" is the average of the 9 sectors. (For interpretation of the references to color in this figure legend, the reader is referred to the Web version of this article.)

Sliding is allowed only where basal temperatures are at or near the pressure melt point, just as for sediment deformation and quarrying described above. C and τ_b in (2) are just for sliding over exposed bedrock, where sediment thickness is non-existent or thin (< 0.5 m). For sediment thicknesses between 0 and 0.5 m, sediment patchiness depends linearly on its cell-mean thickness, and a cell-mean basal sliding coefficient is calculated for the ice dynamics, which allows for two distinct sub-grid basal shear stresses over sediment patches vs. exposed bedrock patches, but with the same basal ice sliding velocity ν_b across the whole grid cell (Pollard and DeConto, 2007).

Before the inception of major ice on Antarctica ~34 Ma, a thick regolith is expected to have developed during the tens of millions of years of earlier mostly ice-free conditions (as assumed for North America before ~3 Ma in Clark and Pollard, 1998). This is represented by modifying the physical properties of the initial upper bedrock (which is preferable to including it in the sediment model, so that all modeled sediment derives from post 40 Ma erosion of bedrock). In all simulations, relatively large regolith-like values of basal sliding coefficient C and quarrying rate coefficient k are imposed in the bedrock model until the cumulative quarried thickness of bedrock from the start of the run reaches a certain depth at each grid point. This depth is 20 m over initial land (i.e., where bed elevation is above sea level at the start of the run), with $C = 10^{-9}$ m y⁻¹ per Pa² and $k = 10^{-9}$ m y⁻¹ per (Pa m y ¹). When cumulative quarrying exceeds this depth, (i.e., all regolith has been eroded at that grid point), basal sliding coefficients C are set to the value in the pattern deduced by a prior inverse procedure fitting to the modern ice-sheet thickness (Pollard and DeConto, 2012b). Also when cumulative quarrying exceeds the initial regolith depth, the quarrying coefficient k is set to a uniform value representing tougher bedrock, which is adjusted as described below, with values typically $\sim 10^{-11}$ to 10⁻¹⁰ m y⁻¹ per (Pa m y⁻¹).

Similarly, an initial thickness of 100 m of pre-40 Ma oceanic "sediment" is assumed for ocean-covered bedrock (i.e., where bedrock elevations are below sea level at the start of the run), by using $C=10^{-6}$ m y⁻¹ per Pa²and $k=10^{-9}$ m y⁻¹ per (Pa m y⁻¹) at those locations in the bedrock model. After (and if ever) the cumulative quarrying has eroded this thickness, k is set to the same uniform value for land as above. Note

that this rarely occurs during the simulations, because in distal ocean regions the initial pre-existing oceanic sediment is never eroded, and in proximal ocean regions, it is replaced or overlain by thick layers of model-generated post-40 Ma sediment.

2.4. Climate forcing

The climate forcing in the long runs here needs to be specified efficiently; global or regional climate model snapshots at regular intervals would not be computationally feasible. An alternative method would be to use a matrix of preliminary climate model solutions, but that has other drawbacks as discussed in Pollard (2010). Here we simply use modern climatological atmospheric and oceanic datasets for Antarctica, perturbed for past times by spatially uniform offsets that depend simply on a geologic proxy record of atmospheric CO₂ (Zhang et al., 2013) and orbital insolation variations (Laskar et al., 2004). After 2.5 Ma, the influence of Northern Hemispheric glacial cycles is added depending on a deep-sea-core δ^{18} O stack (Lisiecki and Raymo, 2005). All of the external forcing curves are shown in Fig. 1. Details of the atmospheric and oceanic climate forcing parameterizations are given in the Supplementary Material, including the coefficients applied to each of the forcings in Fig. 1, and additional albedo feedback of Antarctic ice.

3. Typical 40 Myr simulation: ice sheet evolution

Results are shown here for one representative long-term simulation, run continuously from 40 Ma to the present, with initial bedrock elevations at 40 Ma set to the geologic reconstruction for 34 Ma of Wilson et al. (2012). This assumes erosion between 40 and 34 Ma is minor; in all our simulations, this is the case, with very little ice and insignificant erosion before 34 Ma. Many such runs were performed at 80 and 160 km resolutions, varying mainly important parameters involved in the climate forcing, and the one shown here is typical of those with the better fits to the observed events and trends in Cenozoic Antarctic Ice Sheet evolution outlined in the introduction. This section briefly describes the model ice-sheet evolution and correspondence to observations, and model-data misfits indicating the need for future work.

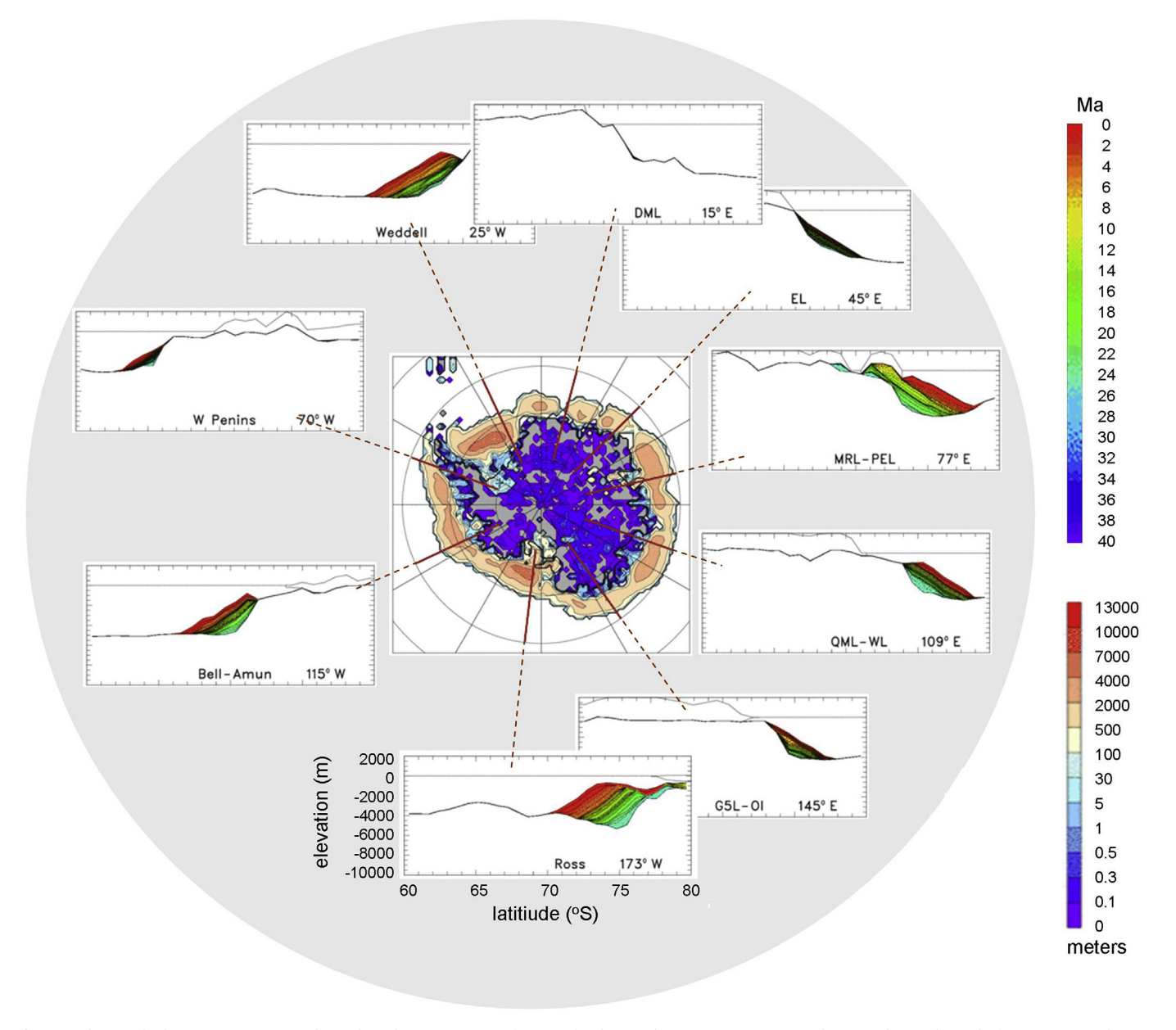


Fig. 7. Sediment thickness, (meters, central panel) and cross sections of times of sediment deposition (Ma, surrounding panels), at the end of a 40 Myr simulation. Each cross section runs from 80 to 60 °S, along a line of constant longitude that corresponds roughly with the centerline of a sector in Fig. 6a. In each cross-section panel, the vertical axis is elevation relative to sea level, from -10000 to 2000 m, as shown in the lowermost panel for the Ross. The flat horizontal line at 0 m elevation is sea level, and the black line running immediately below and beyond the colored sediment strata is bedrock elevation. The other black lines show the modern ice sheet surface, and the base of floating ice if any. For reference, the following publications include observed seismic profiles that roughly match the locations of the model cross sections (although much shorter in length): DML: Leitchenkov et al. (2008). EL: Stagg et al. (2004). MRL-PEL: Jamieson et al. (2005). QML-WL: Gulick et al. (2017). G5L-OL: Close et al. (2007). Ross: Colleoni et al. (2018a). Amundsen: Gohl et al. (2013). Bellingshausen: Uenzelmann-Neben (2018). W. Peninsula: Rebesco et al. (1996). Weddell: Bart et al. (1999).

As seen in the ice-volume time series in Fig. 2 and the snapshots of ice distributions in Fig. 3, the inception of ice at the Eocene-Oligocene boundary ~ 34 Ma is too small, and major ice growth does not occur until ~ 26 Ma. We were unable to improve this aspect by adjusting the CO_2 and albedo-feedback coefficients of the atmospheric forcing, or by variations in initial bedrock topography (see Supplementary Material). We ascribe this shortcoming to a combination of:

- The proxy record of atmospheric CO₂ possibly not being realistic in the few million years before and after 34 Ma (Zhang et al., 2013).
 Higher CO₂ values before, and a deeper drop to longer-lasting lower values after, would produce earlier and more sudden ice growth (DeConto and Pollard, 2003; Pollard and DeConto, 2005). Using
- alternate CO_2 variations with these properties can produce more realistic ice-sheet inceptions in the model (see Supplementary Material).
- 2) Different hysteresis properties of equilibrium ice volume vs. climate in the coarse-resolution ice sheet model here, compared to finer-resolution versions (DeConto and Pollard, 2003; Pollard and DeConto, 2005). The hysteresis in the current model is considerably less than the earlier model. This hysteresis depends strongly on the slope of the snowline vs. latitude (less hysteresis with smaller slope as in the climate forcing here), and so tends to reduce the amplitude and permanence of continental ice onset in the current runs. Also, the coarse horizontal resolution may be directly affecting these aspects (van den Berg et al., 2006; Gasson et al., 2016).

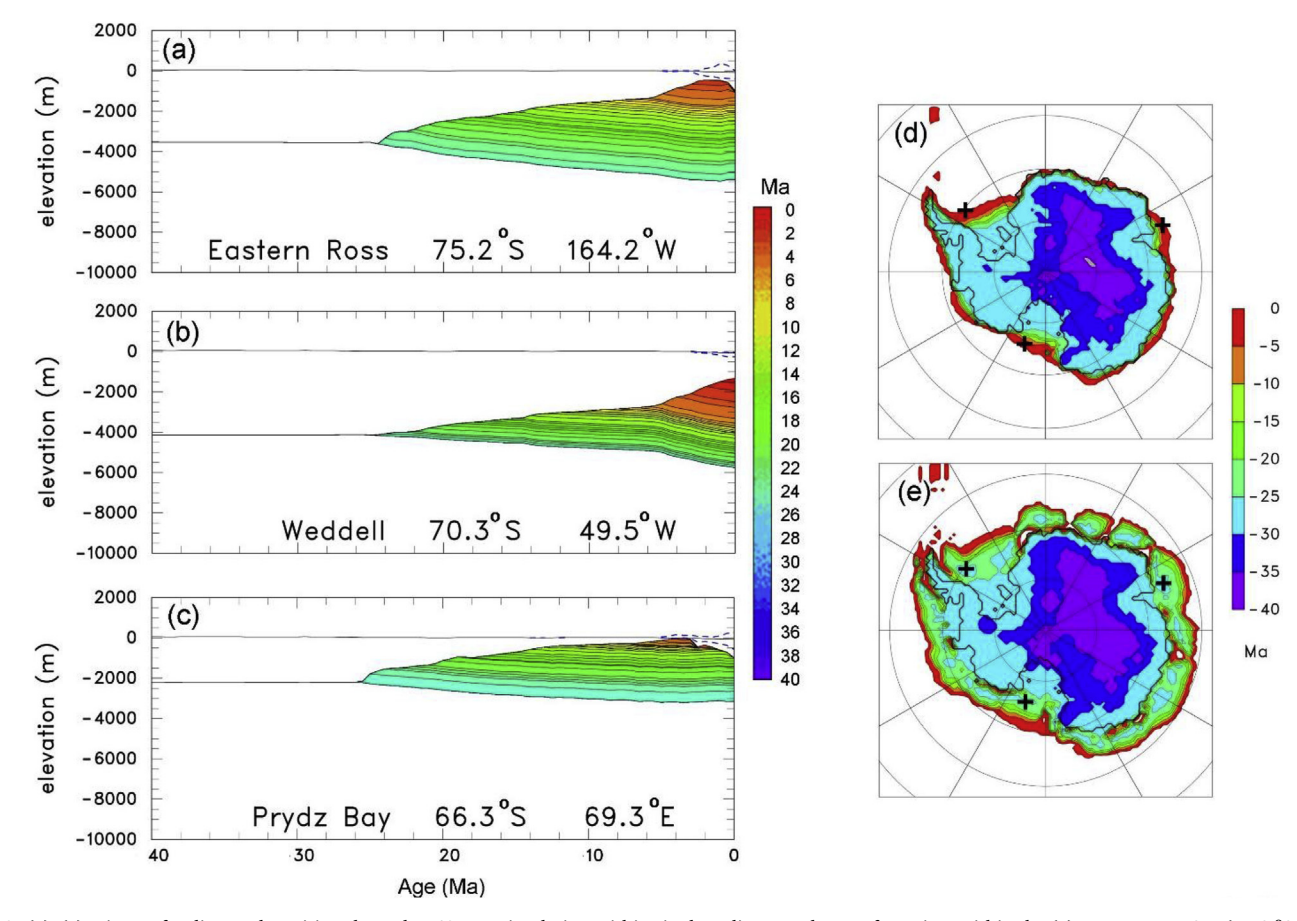


Fig. 8. (a)–(c): Times of sediment deposition through a 40 Myr simulation within single sediment columns, for points within the (a) Eastern Ross Sea (75.2 °S, 164.2 °W), (b) Weddell Sea (70.3 °S, 49.5 °W), and (c) Prydz Bay (66.3 °S, 69.3 °E). Dashed blue lines show the surface and base of ice when present, smoothed with a running-mean window of 200 kyrs. (d) Time of first presence of grounded ice at each location (Ma), during the simulation. (e) Time of first occurrence of deposited sediment at each location (Ma), during the simulation. The locations of the sites in (a–c) are shown by black crosses in panels (d) and (e).

We plan to continue to work on the Eocene-Oligocene transition in these long-term studies. It may be that appropriate adjustments of (i) ${\rm CO}_2$ forcing, (ii) amounts of initial regolith, (iii) climatic snowline slopes, and (iv) finer model resolution, may yield more realistic ice growth at the Eocene-Oligocene boundary. For now, the shortcomings early in the Eocene and Oligocene have little effect on the model's bedrock state toward the end of the runs, and on total quarrying and modern marine sediment distributions, as described below.

Another deficiency seen in Fig. 2a is the failure to simulate smaller ice volumes during the Middle-Miocene Climatic Optimum (MMCO, $\sim\!17$ to 15 Ma) as implied by deep-sea-core $\delta^{18}\text{O}$ records. Stap et al. (2016) found that lowering of Antarctic bedrock elevations by glacial erosion since the Eocene-Oligocene has the potential to produce smaller ice sizes during the MMCO; our model includes this basic mechanism (especially in the lowering of the West Antarctic basin from sub-aerial to marine, Wilson et al., 2013), but realistic MMCO ice reductions may also require variations in ocean forcing (Colleoni et al., 2018b; Levy et al., 2019).

As shown in Figs. 2 and 3, the simulation of Plio-Pleistocene glacial-interglacial cycles is reasonably successful. However, there are clearly large errors in the modeled final (modern) ice sheet and bedrock state (Figs. 3, and Fig. 5 below), motivating development of the iterative method described later in sections 6 and 7.

4. Typical 40 Myr simulation: sediment and quarrying distributions

For the typical simulation described here, the bedrock quarrying

coefficient k in Eq. (1) was set uniformly in space to 0.436×10^{-10} m y^{-1} per (Pa m y^{-1}). This yields a total volume of modern circum-Antarctic marine sediment ($13.43 \times 10^6 \, \mathrm{km}^3$) which is reasonably close to observed (taken as $13.05 \times 10^6 \, \mathrm{km}^3$, the average of the minimum and maximum estimates in Wilson et al., 2012). This k value was determined by a simple search with a few prior 40 Myr runs.

The thickness of sediment deposits, and the net quarried amounts of bedrock (erosion depth) since the beginning of the run, are shown for selected times in Fig. 4. As described above, this is all post-40 Ma till, quarried from exposed bedrock under the ice. The till is transported in the upper deforming levels (10's of cm) due to ice-sheet basal stress, and deposited usually at or near the grounding line. The overall result is net bedrock erosion in continental regions that remain mostly ice-covered, and thick sediment deposits on the continental shelves where grounding lines fluctuate a large proportion of the time. In a secondary process, sediment is transported further offshore into the deeper Southern Ocean by slumping beyond a maximum slope, which simply represents turbidity currents as described above. Time series of domainwide total bedrock erosion and sediment volume are also shown in Fig. 2.

The overall distribution of modern sediment deposits in Fig. 4d have some correspondence with the broad picture of modern observed amounts, with thick concentrations in some sectors of the continental shelf (maps shown for instance in Leitchenkov et al., 2007, 2008; Whittaker et al., 2013; Huang et al., 2014; Wobbe et al., 2014; Lindeque et al., 2016a,b; further references for Table 1 in Wilson et al., 2012). Sediment is conserved in the model, i.e., the total sediment volume in Fig. 4d is exactly equal to the total volume of quarried bedrock over the

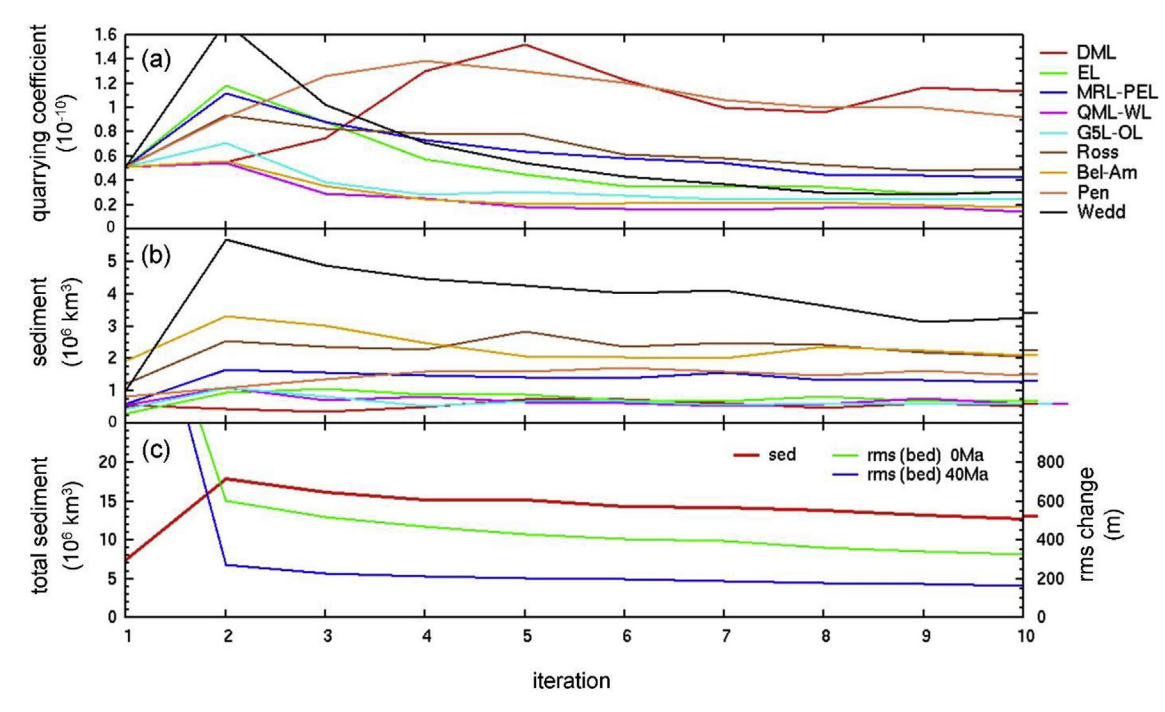


Fig. 9. Convergence of the iterative procedure towards observed sediment totals and modern bedrock elevations (see text). (a) Quarrying coefficient (*k* in Eq. (1), x 10^{-10} m y⁻¹ per (Pa m y⁻¹) for individual sectors as labelled at right, and shown in Fig. 6a. (b) total modern sediment volumes, 10^6 km³, for the individual sectors. Short line segments to the right of the panel are the corresponding observed estimates in Wilson et al. (2012), averages of their maximum and minimum values. (c) Red: total domain-wide modern sediment volume, 10^6 km³. Short line segment to the right shows the total observed estimate (Wilson et al., 2012, averaged as above). Blue: domain-wide rms adjustment in the initial (40 Ma) bedrock elevations between iterations, meters (right-hand axis). Green: domain-wide rms difference of modern rebounded bedrock elevations between successive iterations, meters (right-hand axis). (For interpretation of the references to color in this figure legend, the reader is referred to the Web version of this article.)

run (times the density ratio ρ_b/ρ_s) in Fig. 4h. The distribution of post-Eocene quarried bedrock, i.e., erosion depths, in Fig. 4h is in broad agreement with other geologically based studies (Jamieson et al., 2010; Wilson et al., 2012), except in central West Antarctica where the modeled total erosion (\sim 500–1000 m) is considerably less than in Wilson et al. (2012) (\sim 2000 m, their Fig. 5); this is compensated in the total amounts by our erosion being much deeper (several km) and concentrated in marine outlets around the coast.

The hypsometries of rebounded bed elevations with no ice at the start and end of the run are shown in Fig. 5. "Rebounded" beds are used (i.e., adjusted for simple local isostatic adjustment with all ice removed) to minimize the effects of errors in the model's modern ice. The 40 Ma hypsometry (blue curve) is just that of the prescribed initial state (average of Wilson et al.'s (2012) minimum and maximum reconstructions). The main change over the 40 My simulation is due to glacial erosion of bedrock from interior elevation bins between ~0 and 1600 m (40 Ma, blue curve), transferred to sediment in oceanic elevation bins between -200 and -2000 m (modern, thick red curve). The overall character of the modern hypsometry agrees with observed, but with significant differences (thin red curve, from Bedmap2; Fretwell et al., 2013). When the iterative procedure is used, the modern hypsometry becomes more realistic, as shown in the Supplementary Material.

As mentioned above, the quarrying coefficient k for this run was adjusted to yield the observed total modern sediment volume, but was held uniform in space for all of Antarctica. The totals for individual drainage basins are shown in Fig. 6b, and compared with observed totals (averages of Wilson et al., 2012's minimum and maximum values from their Table 1, which were estimated from modern sediment surveys, and with basin outlines based on modern drainages as shown in Fig. 6a). Most of the individual basin sediment volumes are in rough agreement with observed, despite the uniform value of the quarrying coefficient k in Eq. (1). The agreement with observed basin sediment

volumes improves further when the iterative procedure is used to set k individually for each basin (see the Supplementary Material). As mentioned above variations in k implicitly represent regional variations in bedrock properties, which are largely unknown from direct observations

5. Typical 40 Myr simulation: sediment strata, cross sections

During the runs, the times (in Ma) of deposition of sediment in each cell are recorded, as the sediment column thickness increases through regular 10-m increments. If the sediment column thins (from the top, due to net sediment transport out of the cell), and the column thickness decreases through a 10-m increment, the previously recorded time is erased. The array of these times vs. x,y,z constitutes a continental-wide 3-D map of sediment strata (after adding the 10-m vertical scale to the absolute elevation of the sediment base), for any time during the run. Cross-sections of the modern map at the end of a 40 Myr run can be plotted for any chosen x,y transect, and compared with published seismic profiles for that transect. Note that the model profiles only include sediment eroded since 40 Ma, subsequently deposited and potentially further transported by ocean currents, so should be compared only with observed sediments above that horizon. Sediments eroded and deposited before 40 Ma (or approximately 34 Ma) observed in seismic profiles (e.g., Gohl et al., 2013, their units ASS-1 and ASS-2) correspond to "bedrock" in the model below all model sediment.

A selection of these modern cross sections is shown in Fig. 7, each running along longitudinal meridians from 60 to 80 $^{\circ}$ S. The longitudes correspond roughly to the center lines of the basins defined in Wilson et al. (2012) and used in Fig. 6 above. Common features in the model transects are:

 Most sediment is deposited after ~24 Ma, during and after the Miocene. There is little deposition in the Oligocene when the ice

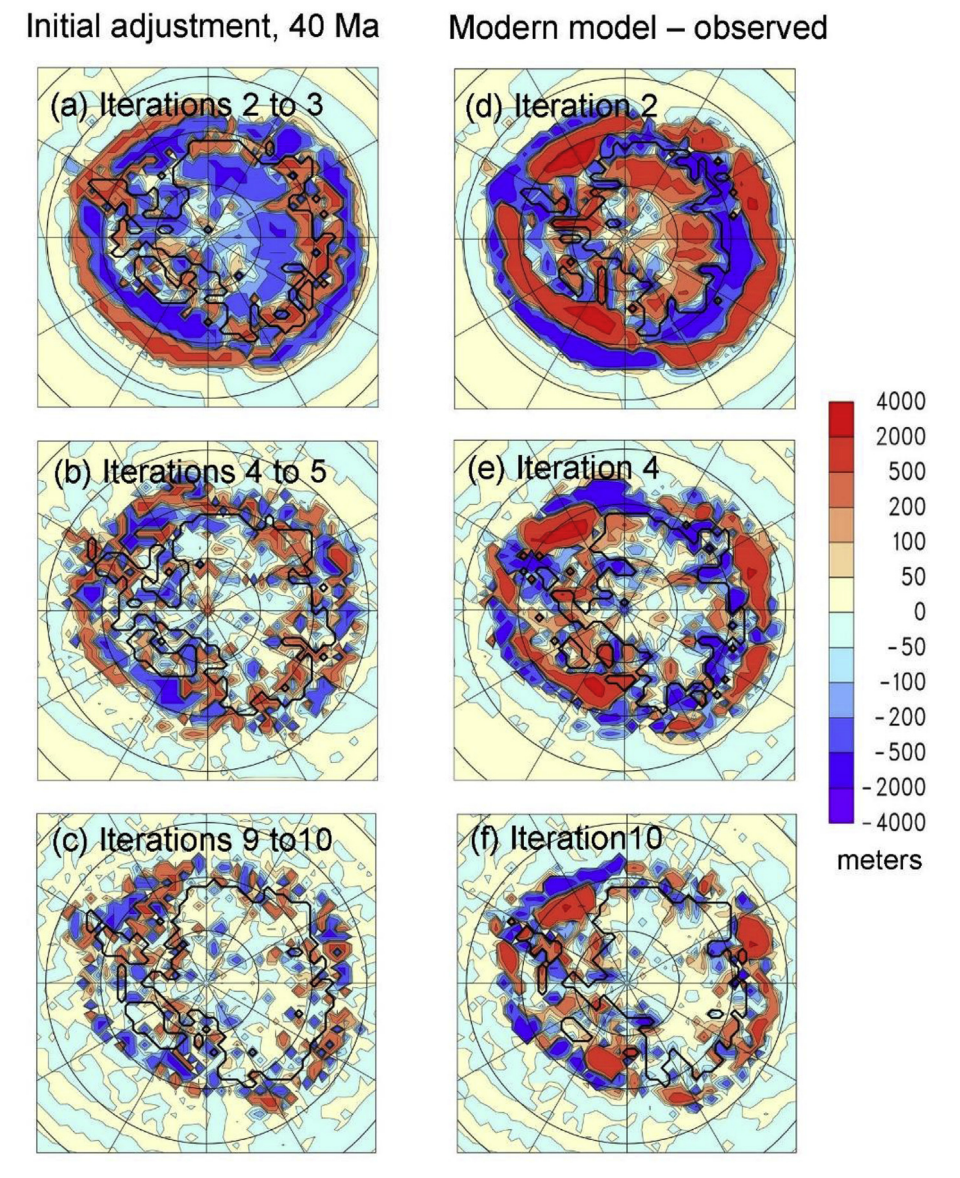


Fig. 10. (a)–(c): Adjustments applied to initial bedrock elevations at the start of selected iterations, meters. This is $h_b - h_{b,pre}$; see Eq. (S3.3) of the Supplementary Material. (d) to (f): Model minus observed (from Bedmap2, Fretwell et al., 2013) error in modern ice-free rebounded bedrock elevations at the end of selected iterations, meters. This is $h_{b,reb,mod} - h_{b,reb,obs}$; see Eq. (S3.3) of the Supplementary Material.

sheet was more confined to terrestrial margins and did not expand often over the continental shelves.

- (ii) Offshore of major basins (Ross, Weddell, Amundsen, Prydz), there are prograding sequences from the Miocene to the present.
- (iii) In the major basins, retrograde surface slopes form on the inner continental shelves, with unconformities as older sediment is removed in the late Miocene to Pleistocene. However in some basins there is an unrealistic peak in the mid shelf region.
- (iv) There are distinct shelf breaks, sloping steeply to the deep ocean at many sites, due partly to slumping in the model representing turbidity currents (section 2.2 and Supplementary Material).

The above features have some correspondence with observed profiles, shown in many individual papers for these and nearby transects (sample references are given in the figure caption). However, there are clearly some first-order mismatches and shortcomings in the model transects. For instance, the retrograde slope in the Ross Sea transect extends too far north, and the real shelf break and slope are located some 100–200 km further south (Colleoni et al., 2018a). It is challenging to make more quantitative comparisons, because of the limited

length of most profiles (much shorter than the $\sim\!2000\,\mathrm{km}$ long model transects), and uncertain dating of many observed strata and unconformities. However, in further work we hope that systematic comparisons with representative profiles around Antarctica can help to assess and improve the model, for instance using the Antarctic Seismic Data Library System SDLS, http://sdls.ogs.trieste.it/.

Figs. 8a–c shows another type of cross-section for a single location, that can be generated from the saved array of sediment times. Here the times of deposition within the sediment column are plotted vs. time through the run. Although this type of plot does not correspond directly to any observable data product, it can clearly show when major episodes of deposition and erosion occur, at locations of particular interest. At the Prydz Bay site (Fig. 8c) from ~3 Ma to the present, previously deposited sediments are removed from the upper layers of the column (transported downstream by grounded ice), thinning the column. The dashed blue lines in these figures indicate when ice is present, which does not occur at these locations until the mid-Pliocene, near the end of the run. This can also be seen in the spatial maps of first occurrence of grounded ice, and first occurrence of deposited sediment (Fig. 8d, e), which show that grounded ice does not expand across modern

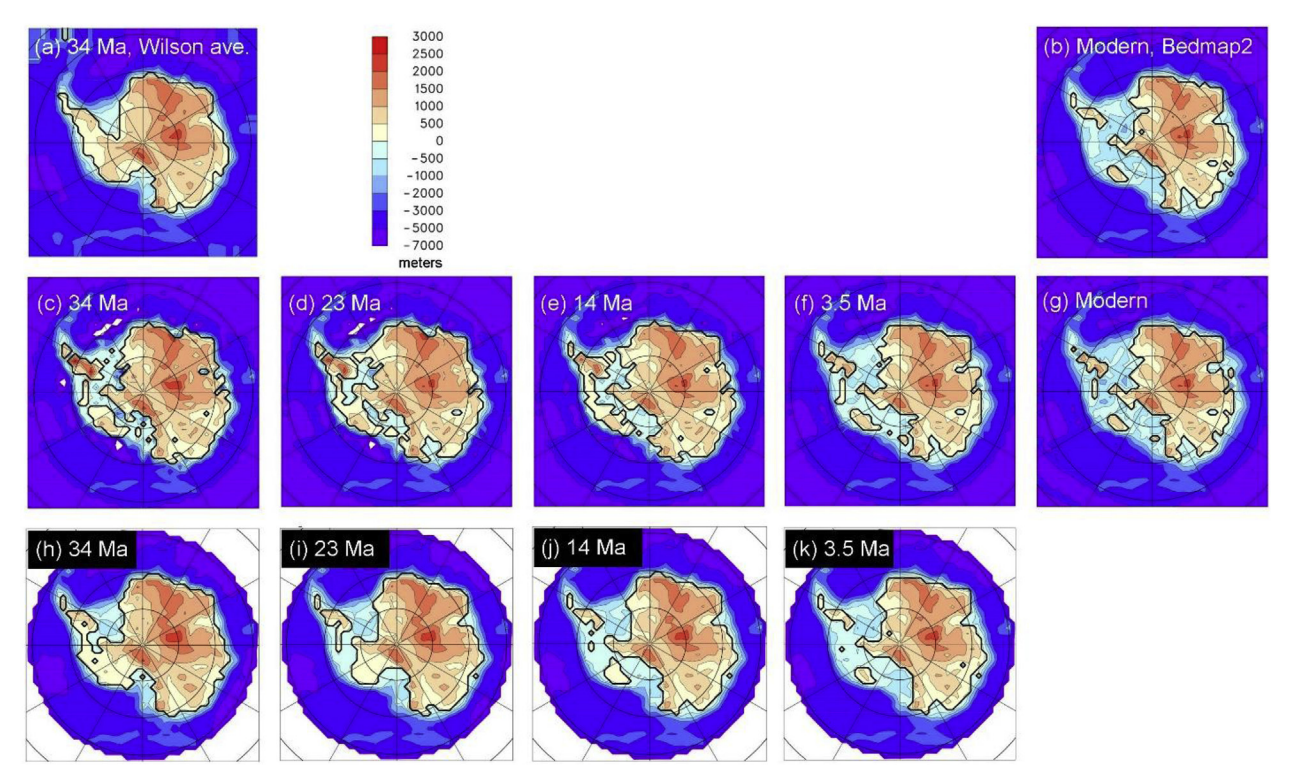


Fig. 11. Maps of ice-free rebounded bedrock elevations (m) at selected times for an iterative simulation and various other sources. (a) Wilson et al. (2012) average of their minimum and maximum 34 Ma reconstructions. (b) Modern observed (from Bedmap2, Fretwell et al., 2013, at 160 km resolution). (c) to (g): Model, during the final (tenth) iteration, for 34 Ma (Eocene-Oligocene), 23 Ma (Oligocene-Miocene), 14 Ma (mid Miocene), 3.5 Ma (mid Pliocene), and modern. (h) to (k): New geologic reconstructions through the Cenozoic (Paxman et al., 2019b; their median reconstructions).

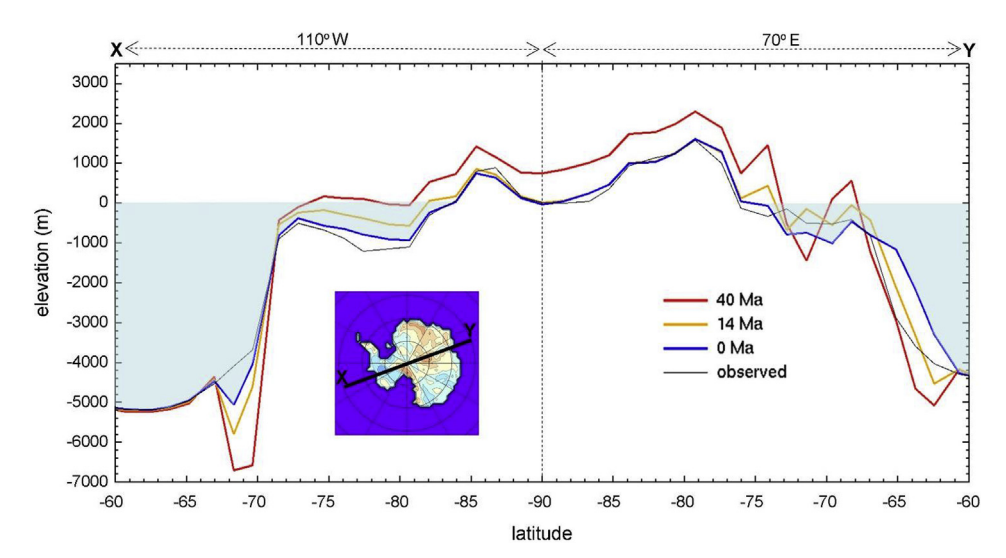


Fig. 12. Transects of bed elevations (meters, including sediment) at selected times during the final run in the iterative simulation. The left half of the figure is along longitude 110°W, and the right half is along longitude 70°E, both running from the pole to 60°S (inset). Red: at 40 Ma (start). Orange: at 14 Ma. Blue: at 0 Ma (modern). Black: modern observed, calculated from Bedmap2 (Fretwell et al., 2013) at 160 km resolution as in the model run. Light blue shading shows the model's modern ocean. The lower bed elevations in the interior regions at 14 and 0 Ma (compared to 40 Ma) are mainly due to the current ice load; much of the lowering due to erosion has been compensated by isostatic relaxation. (For interpretation of the references to color in this figure legend, the reader is referred to the Web version of this article.)

continental shelves until the last few million years of the run. But sediment expands sooner, from early deposits further inland, due to the model's slumping process representing turbidity currents.

6. Iterative procedure for quarrying coefficients and initial bedrock

In the typical simulation described above in sections 3 to 5, the initial bedrock topography at 40 Ma was based on Wilson et al.'s (2012) reconstructions for 34 Ma (the average of their minimum and maximum maps). Their geologic reconstructions are based in part on restoring modern marine sediments back onto the interior bed, mostly in West Antarctica. In our work the post-Eocene sediment transfer is simulated

explicitly, and modern sediment volume is one of the metrics used in testing the model, so the use of their reconstruction as initial conditions may be regarded as somewhat circular.

We developed an alternate iterative procedure that partially addresses this concern. The model is repeatedly run through the last 40 Myr, and the initial Antarctic bedrock topography of the first iteration can be set arbitrarily (to an axisymmetric cone in our case). Both the initial bedrock topographic map and the basin-specific bedrock quarrying coefficients are adjusted between the runs, based on misfits between modern observations and the previous run's final state, in: (i) total post-Eocene marine sediment volumes in individual basins (Wilson et al., 2012) as in Fig. 6b, and (ii) modern bed elevations after isostatic rebound with all ice removed (Bedmap2, Fretwell et al., 2013)

as in Fig. 10d–f below. The misfits in (i) and (ii) determine adjustments to (a) bedrock quarrying coefficients and (b) initial bedrock topography at 40 Ma, for the next run.

The adjustments of quarrying coefficients to match total sediment volumes in each sector has a counterpart in Wilson et al. (2012), who did the same "in reverse" with their ice-sheet modeling determining where to restore the sediment at 34 Ma. The adjustment of initial bed topography is analogous to the "outer iteration" made in coupled ice-Earth-sea level model paleo-simulations (Gomez et al., 2013; Kendall et al., 2005).

At each iteration, adjustments to quarrying coefficients are made first, attempting to match the observed modern sediment volume for each basin, under the assumptions that total quarrying is proportional to the quarrying coefficient and that sediment remains within the basin. Then, adjustments to initial bedrock topography are made by (i) cancelling out the error in modern topography vs. observed in the previous run, and (ii) allowing for anticipated changes throughout the next run due to the adjustments in quarrying coefficients, which change the total amounts of bedrock erosion, sediment, and thus modern topography. The topographic adjustments are done point-by-point using quantities at individual grid cells from the previous run. This does not exactly have the desired effect of course, due to spatial interactions with ice dynamics and sediment transport, but may be close enough to allow multiple iterations to converge. Further details and equations governing the adjustments at each iteration are given in the Supplementary Material.

7. Results with iterative procedure

This section present results of a simulation using the iterative procedure described above. We performed 10 iterations for most experiments, and results are shown here for the last iteration. As shown below, convergence is adequate after this number of iterations, but is weak in some cases, and consequently we did not use any formal convergence criteria. To reduce wall-clock requirements, a very coarse horizontal resolution was used, 160 km, compared to 80 km in the single simulation presented above. Sensitivity tests (not shown) indicate that results are changed only slightly by the coarser resolution, and the major features and conclusions in this paper are unchanged.

The convergence of the iterative procedure is described in Figs. 9 and 10. Fig. 9 shows how various aggregate quantities change rapidly over the first few iterations and then asymptote towards their close-toconverged final values. As mentioned above, the first iteration starts with arbitrarily defined bedrock topography, here an idealized axisymmetric cone centered on the South Pole with linear slopes vs. latitude, so the first adjustments of bedrock topography are very large. (Another choice for the starting topography could be from Wilson et al. (2012) as in the non-iterative experiment above, but the cone yields essentially the same final results, and demonstrates that the procedure can be independent of geologic reconstructions). After the "jolt" of the first iteration, most of the adjustments are completed after ~5 iterations, but the rms adjustments to initial topography, and rms differences from modern topography, continue to decrease slowly for another ~5 iterations (Fig. 9c, blue and green curves). Most quarrying coefficients asymptote smoothly (Fig. 9a); those for Dronning Maud Land and the Peninsula do not, but continue to settle down in experiments with more iterations (up to 20, not shown). Total sediment volumes for each sector successfully converge on their observed targets (Fig. 9b).

Spatial maps of initial (40 Ma) adjustments and final (modern) errors in rebounded bedrock elevations in Fig. 10 show clear reductions of magnitudes over the iterative sequence. However, the convergence to modern bedrock elevations is not entirely successful; there are still large patches with errors greater than $\sim\!500\,\mathrm{m}$ remaining at the end of the final (tenth) iteration (Fig. 10f). These errors are located offshore from major basins on the continental slope and rise, where the bed descends steeply from the continental shelf to $>3000\,\mathrm{m}$ in the abyssal

ocean, and so may reflect relatively small displacements in the model slope (Fig. 11g vs b). Further iterations reduce the size and magnitude of these errors slightly but not substantially (not shown). We have experimented with modified iteration procedures, such as correcting initial bedrock elevations or quarrying coefficients separately and not simultaneously, but with only incremental improvements in convergence.

In principle, one end product of the procedure is a set of bedrock elevation maps for 40 Ma and any time since, independent of geologic reconstructions. Fig. 11c-g shows the model's ice-free rebounded bedrock topographies for selected times during the last iteration. However, this is very preliminary and the results shown here undoubtedly contain large model errors. Biases in the model physics can be masked as cancelling errors by the iteration, so for the converged results to be meaningful, all physical biases must be small. This includes errors in the simple climate forcing, sediment processes (notably ice-entrained vs. deforming transport), and ice dynamics. Also there are strong nonlinear feedbacks between ice, sediment and bedrock that complicate the assessment of model vs. data; for instance, the distribution of sediment under grounded ice affects basal sliding and ice distribution, which in turn influences bedrock erosion and generation of later sediment.

Nevertheless, the model maps in Fig. 11c-g can be compared with geologically based reconstructions, such as Wilson et al. (2012) for 34 Ma (Fig. 11a), Gasson et al. (2016) for 20 Ma, Paxman et al. (2019b) for various times (Figs. 11h-k), and modern observed (Bedmap2, Fretwell et al., 2013, Fig. 11b). There is first-order agreement with some aspects of these maps, such as the overall transition from subaerial to submerged bedrock in West Antarctica, seen also in a transect across all of Antarctica in Fig. 12, which also illustrates the overall creation or seaward expansion of continental shelves (cf. Hochmuth and Gohl, 2019). However, the model underestimates the extent of subareal land at 34 Ma (Fig. 11c vs 11a,h), and the transition to submerged bedrock is not monotonic everywhere, with maximum subaerial extents in West Antarctica occurring around 23 Ma (Fig. 11d), due presumably to early sediment buildup outpacing thermal subsidence. After further model improvement, we hope to make more meaningful comparisons between these model-generated maps and paleo topographic reconstructions during the Cenozoic, such as Paxman et al. (2019b).

8. Conclusions

With some compromises, time-continuous simulations with a 3-D Antarctic ice and sediment model are feasible over the entire late Cenozoic, from major ice-sheet inception around $\sim\!\!34\,\mathrm{Ma}$ to modern. The main compromise needed to reduce run times is coarse horizontal resolution, 80–160 km (compared to 10–20 km commonly used for much shorter continental-scale simulations). A second compromise is the use of very simple climate forcing, with spatially uniform shifts from modern climatology in proportion to orbital insolation variations and geologic records of atmospheric CO₂, and deep-sea-core $8^{18}\mathrm{O}$ representing the influence of Northern Hemispheric glaciation during the last $\sim\!\!3\,\mathrm{Myr}$

A numerical technique is described to produce 3-D maps of the ages of sediment deposition vs. depth. Cross sections of this map can be compared directly with the extensive body of published seismic profiles on Antarctic continental shelves. A few sample cross sections are shown here; more systematic assessments vs. published profiles are deferred to future work, hopefully making use of profile databases such as the Antarctic Seismic Data Library System SDLS, http://sdls.ogs.trieste.it/.

The initial 40 Ma bedrock topography can be prescribed from geologically based reconstructions. Alternatively an iterative procedure can be used involving multiple runs over the whole 40 Myr period, adjusting quarrying coefficients and initial topography to better fit observed bedrock elevations and post-Eocene sediment volumes. The iterative procedure produces model-generated paleo-topographic maps,

independent of geologic reconstructions. Examples are shown for selected times, which in principle can be compared and assessed with geologic reconstructions. However, considerable progress to reduce model uncertainties will likely be needed before useful comparisons can be made, for instance in the mode of sediment transport (entrainment in basal ice, deforming as here, or ploughing), interactions with basal hydrology, and omitted processes such as sediment compaction and mantle-driven dynamic topography. Other uncertainties stem from the iterative procedure itself. Although it provides the capability of correcting biases in modern elevations by adjusting the initial 40 Ma topography, more work is needed to tell whether these adjustments are based in reality or are just cancelling errors in the model physics (see the Supplementary Material section 4).

The model follows in the vein of previous studies of late-Cenozoic evolution of Antarctic ice, and can be tested against specific events and trends mentioned in the introduction. Although the preliminary results agree with several first-order aspects of observed events, substantial deficiencies remain. These include the Eocene-Oligocene transition, and reduced ice during the Middle-Miocene Climatic Optimum (see section 3 and the Supplementary Material section 2). Further work will be aimed at refining the model to improve these aspects, progressing towards realistic time-continuous simulations through the whole late Cenozoic.

Acknowledgements

We thank two anonymous reviewers for careful and constructive reviews, and Karsten Gohl and Katharina Hochmuth for helpful suggestions. We also thank Douglas Wilson for providing maps of West Antarctic thermal subsidence and Antarctic basin boundaries as in Wilson et al. (2012), including a boundary between the Amundsen and Ross basins that does not appear in their Fig. 4. The atmospheric CO₂ record of Pagani et al. (2005) used in the Supplementary Material was obtained from the Palaeo-CO₂ Project website http://www.p-co2.org. This work was supported in part by US National Science Foundation grants GEO-1240507 and ICER-1663693.

Appendix A. Supplementary material

Supplementary material to this article can be found online at https://doi.org/10.1016/j.palaeo.2019.109374.

Declarations of interest

None.

References

- Anderson, J.B., 1999. Antarctic Marine Geology. Cambridge University Press, pp. 289.
 Austermann, J., Pollard, D., Mitrovica, J.X., Moucha, R., Forte, A.M., DeConto, R.M.,
 Rowley, D.B., Raymo, M.E., 2015. The impact of dynamic topography change on
 Antarctic Ice Sheet stability during the mid-Pliocene warm period. Geology 43, 927–930.
- Barrett, P., 1996. Antarctic palaeoenvironment through Cenozoic times a review. Terra Antarctica 3 (2), 103–119.
- Bart, P.J., de Batist, M., Jokat, W., 1999. Interglacial collapse of crary trough-mouth fan, Weddell Sea, antartica: implications for antartic glacial history. J. Sediment. Res. 69, 1276–1289.
- Bart, P.J., Mullally, D., Golledge, N.R., 2016. The influence of continental shelf bathymetry on Antarctic Ice Sheet response to climate forcing. Glob. Planet. Chang. 142, 87-05
- Bougamont, M., Tuylaczyk, S., 2003. Glacial erosion beneath ice streams and ice-stream tributaries: constraints on temporal and spatial distribution of erosion from numerical simulations of a West Antarctic ice stream. Boreas 32, 178–190.
- Brinkerhoff, D., Truffer, M., Aschwanden, A., 2017. Sediment transport drives tidewater glacier periodicity. Nat. Commun. 8. https://doi.org/10.1038/s41467-017-00095-5.
- Clark, P.U., Pollard, D., 1998. Origin of the mid-Pleistocene transition by ice-sheet erosion of regolith. Paleoceanography 13, 1–9.
- Close, D.I., Stagg, H.M.J., O'Brien, P.E., 2007. Seismic stratigraphy and sediment distribution on the wilkes land and terre adelie margins, East Antarctica. Mar. Geol. 239, 33–57.

- Cooper, A.K., Eittreim, S., ten Brink, U., Zayatz, I., 1993. Cenozoic glacial sequences of the Antarctic continental margin as recorders of Antarctic ice sheet fluctuations. In: In: Kennett, J.P., Warnke, D.A. (Eds.), The Antarctic Paleoenvironment: A Perspective on Global Change, Part Two, vol. 60. American Geophysical Union, Washington D.C., pp. 75–89 Antarctic Research Series.
- Cramer, B.S., Toggweiler, J.R., Wright, J.D., Katz, M.E., Miller, K.G., 2009. Ocean over-turning since the Late Cretaceous: inferences from a new benthic foraminiferal isotope compilation. Peleoceanography 24, PA4216. https://doi.org/10.1029/2008PA001683.
- Colleoni, F., De Santis, L., Siddoway, C.S., Bergamasco, A., Golledge, N.R., Lohmann, G., Passchier, S., Siegert, M.J., 2018a. Spatio-temporal variability of processes across Antarctic ice-bed-ocean interfaces. Nat. Commun. 9 (1), 2289. https://doi.org/10. 1038/s41467-018-04583-0.
- Colleoni, F., De Santis, F., Montoli, E., Olivo, E., Sorlien, C.C., Bart, P.J., Gasson, E.G.W., Bergamasco, A., Sauli, C., Wardell, N., Prato, S., 2018b. Past continental shelf evolution increased Antarctic ice sheet sensitivity to climatic conditions. Sci. Rep. 8, 11323. https://doi.org/10.1038/s41598-018-29718-7.
- de Boer, B., van de Wal, R.S.W., Bintanja, R., Lourens, L., Tuenter, E., 2010. Cenozoic global ice-volume and temperature simulations with 1-D ice-sheet models forced by benthic d18O records. Ann. Glaciol. 51 (55), 23–33.
- de Boer, B., van de Wal, R.S.W., Lourens, L.J., Bintanja, R., 2012. Transient nature of the Earth's climate and the implications for the interpretation of benthic d18O records. Palaeogeogr. Palaeoclimatol. Palaeoecol. 335–336, 4–11.
- de Boer, B. Dolan, A.M., Bernales, J., Gasson, E., Goelzer, H., Golledge, N.R., Sutter, J., Huybrechts, P., Lohmann, G., Rogozhina, I., Abe-Ouchi, A., Saito, F., van de Wal, R.S.W., 2015. Simulating the Antarctic ice sheet in the late-Pliocene warm period: PLISMIP-ANT, an ice-sheet model intercomparison project. The Cryo 9, 881–903.
- De Vleeschouwer, D., Vahlenkamp, M., Crucifix, M., Palike, H., 2017. Alternating Southern and Northern Hemisphere climate response to astronomical forcing during the past 35 m.y. Geology 45, 375–378.
- DeConto, R.M., Pollard, D., 2003. Rapid Cenozoic glaciation of Antarctica induced by declining atmospheric CO₂. Nature 421, 245–249.
- Dowsett, H., Dolan, A., Rowley, D., Moucha, R., Forte, A.M., Mitrovica, J.X., 2016. The PRISM4 (mid-Piacenzian) paleoenvironmental reconstruction. Clim. Past 12, 1519–1538.
- Evans, D.J.A., Phillips, E.R., Hiemstra, J.F., Auton, C.A., 2006. Subglacial till: formation, sedimentary characteristics and classification. Earth Sci. Rev. 78, 115–176.
- Foster, G.L., Rohling, E.J., 2013. Relationship between sea level and climate forcing by CO2 on geological timescales. Proc. Natl. Acad. Sci. 110, 1209–1214.
- Fretwell, P., et al., 2013. Bedmap2: improved ice bed, surface and thickness datasets for Antarctica. The Cryo 7, 375–393.
- Galeotti, S., DeConto, R., Naish, T., Stocchi, P., Florindo, F., Pagani, M., Barrett, P., Bohaty, S.M., Lanci, L., Pollard, D., Sandroni, S., Talarico, F., Zachos, J.C., 2016. Antarctic Ice Sheet variability across the Eocene-Oligocene boundary climate transition. Science 352, 76–80.
- Gasson, E., Siddall, M., Lunt, D., Rackham, O., Lear, C., Pollard, D., 2012. Exploring uncertainties in the relationship between temperature, ice volume and sea level over the past 50 million years. Rev. Geophys. 50 RG1005, 1-35.
- Gasson, E., DeConto, R.M., Pollard, D., Levy, R.H., 2016. Dynamic Antarctic ice sheet during the early to mid-Miocene. Proc. Natl. Acad. Sci. 113, 3459–3464.
- Gohl, K., Uenzelmann-Neben, G., Larter, R.D., Hillenbrand, C.-D., Hochmuth, K., Kalberg, T., Weigelt, E., Davy, B., Kuhn, G., Nitsche, F.O., 2013. Seismic stratigraphic record of the Amundsen Sea Embayment shelf from pre-glacial to recent times: evidence for a dynamic West Antarctic ice sheet. Mar. Geol. 344, 115–131.
- Golledge, N.R., Levy, R.H., McKay, R.M., Fogwill, C.J., White, D.A., Graham, A.G.C., Smith, J.A., Hillenbrand, C.-D., Licht, K.J., Denton, G.H., Ackert Jr., R.P., Maas, S.M., Hall, B.L., 2013. Glaciology and geological signature of the last glacial maximum antarctic ice sheet. Quat. Sci. Rev. 78, 225–247.
- Golledge, N.R., Thomas, Z.A., Levy, R.H., Gasson, E.G.W., Naish, T.R., McKay, R.M., Kowalewski, D.E., Fogwill, C.J., 2017. Antarctic climate and ice-sheet configuration during the early Pliocene interglacial at 4.23 Ma. Clim. Past 13, 959–975.
- Gomez, N., Pollard, D., Mitrovica, J.X., 2013. A 3-D coupled ice sheet-sea level model applied to Antarctica through the last 40 ky. Earth Planet. Sci. Lett. 384, 88–99.
- Greenop, R., Foster, G.L., Wilson, P.A., Lear, C.H., 2014. Middle Miocene climate instability associated with high-amplitude CO2 variability. Paleoceanography 29, 845–853.
- Gulick, S.P.S., Shevenell, A.E., Montelli, A., Fernandez, R., Smith, C., Warny, S., Bohaty, S.M., Sjunneskog, C., Leventer, A., Frederick, B., Blankenship, D.D., 2017. Initiation and long-term instability of the East antarctic ice sheet. Nature 552, 225–229.
- Herman, F., Braun, J., Deal, E., Prasicek, G., 2018. The response time of glacial erosion. J. Geophys. Res.-Earth Surface 123, 801–817.
- Hildes, D.H.D., Clarke, G.K.C., Flowers, G.E., Marshall, S.J., 2004. Subglacial erosion and englacial sediment transport modelled for North American ice sheets. Quat. Sci. Rev. 23, 409–430.
- Hochmuth, K., Gohl, K., 2019. Seaward growth of Antarctic continental shelves since establishment of a continent-wide ice sheet: patterns and mechanisms. Palaeogeogr. Palaeoclimatol. Palaeoecol. 520, 44–54.
- Huang, X., Gohl, K., Jokat, W., 2014. Variability in Cenozoic sedimentation and paleowater depths of the Weddell Sea basin related to pre-glacial and glacial conditions of Antarctica. Glob. Planet. Chang. 118, 25–41.
- Jamieson, S.S.R., Hulton, N.R.J., Sugden, D.E., Payne, A.J., Taylor, J., 2005. Cenozoic landscape evolution of the Lambert basin, East Antarctica: the relative role of rivers and ice sheets. Glob. Planet. Chang. 45, 35–49.
- Jamieson, S.S.R., Hulton, N.R.J., Hagdorn, M., 2008. Modelling landscape evolution under ice sheets. Geomorphology 97, 91–108.
- Jamieson, S.S.R., Sugden, D.E., Hulton, N.J.R., 2010. The evolution of the subglacial

- landscape of Antarctica. Earth Planet. Sci. Lett. 293, 1-27.
- Jamieson, S.S.R., Stokes, C.R., Ross, N., Rippin, D.M., Bingham, R.G., Wilson, D.S., Margold, M., Bentley, M.J., 2014. The glacial geomorphology of the Antarctic ice sheet bed. Antarct. Sci. 26 (6), 724–741.
- Kendall, R.A., Mitrovica, J.X., Milne, G.A., 2005. On post-glacial sea level II. Numerical formulation and comparative results on spherically symmetric models. Geophys. J. Int. 161, 679–706.
- Laskar, J., Robutel, P., Joutel, F., Gastineau, M., Correia, A.C.M., Levrard, B., 2004. A long-term numerical solution for the insolation quantities of the Earth. Astron. Astrophys. 428, 261–285.
- Leitchenkov, G.L., Guseva, Y.B., Gandyukhin, V.V., 2007. Cenozoic environmental changes along the East Antarctic continental margin inferred from regional seismic stratigraphy. In: In: Cooper, A.K., Raymond, C.R. (Eds.), Antarctica: A Keystone in a Changing World - Online Proceedings of the 10th ISAESpp. 4. https://doi.org/10. 3133/of2007-1047.srp005. USGS Open-File Report 2007-1047, Short Research Paper 005.
- Leitchenkov, G., Guseva, J., Gandyukhin, V., Grikurov, G., Kristoffersen, Y., Sand, M., Golynsky, A., Aleshkova, N., 2008. Crustal structure and tectonic provinces of the Riiser-Larsen Sea area (East Antarctica): results of geophysical studies. Mar. Geophys. Res. 29, 135–158.
- Levy, R., Harwood, D., Florindo, F., Sangiorgi, F., Tripati, R., von Eynatteng, H., Gasson, E., Kuhn, G., Tripati, A., DeConto, R., Fielding, C., Field, B., Golledge, N., McKay, R., Naish, T., Olneyk, M., Pollard, D., Schouten, S., Talarico, F., Warny, S., Willmott, V., Acton, G., Panter, K., Paulsen, T., Taviani, M., SMS Science Team, 2016. Antarctic ice sheet sensitivity to atmospheric CO₂ variations in the early to mid-Miocene. Proc. Natl. Acad. Sci. 113, 3453–3458.
- Levy, R.H., Meyers, S.R., Naish, T.R., Golledge, N.R., McKay, R.M., Crampton, J.S., DeConto, R.M., De Santis, L., Florindo, F., Gasson, E.G.W., Harwood, D.M., Luyendyk, B.P., Powell, R.D., Clowes, C., Kulhanek, D.K., 2019. Antarctic ice-sheet sensitivity to obliquity forcing enhanced through ocean connections. Nat. Geosci. 12, 132–137.
- Liebrand, D., Lourens, L.J., Hodell, D.A., de Boer, B., van de Wal, R.S.W., Palike, H., 2011.
 Antarctic ice sheet and oceanographic response to eccentricity forcing during the early Miocene. Clim. Past 7, 869–880.
- Lindeque, A., Gohl, K., Wobbe, F., Uenzelmann-Neben, G., 2016a. Preglacial to glacial sediment thickness grids for the southern pacific margin of West Antarctica. Geochem. Geophys. Geosyst. 17, 4276–4285.
- Lindeque, A., Gohl, K., Henrys, S., Wobbe, F., Davy, B., 2016b. Seismic stratigraphy along the Amundsen Sea to Ross Sea continental rise: a cross-regional record of pre-glacial to glacial processes of the West Antarctic margin. Palaeogeogr. Palaeoclimatol. Palaeoecol. 443, 183–202.
- Lisiecki, L.E., Raymo, M., 2005. A Pliocene-Pleistocene stack of 57 globally distributed benthic δ¹⁸O records. Paleoceanography 20, PA1003. https://doi.org/10.1029/ 2004PA001071
- Luchi, R., Balachandar, S., Seminara, G., Parker, G., 2018. Turbidity currents with equilibrium basal driving layers: a mechanism for long runout. Geophys. Res. Lett. 45, 1518–1526.
- McKay, R.M., Barret, P.J., Levy, R.S., Naish, T.R., Golledge, N.R., Pyne, A., 2016.
 Antarctic Cenozoic climate history from sedimentary records: ANDRILL and beyond.
 Phil. Trans. Roy. Soc. A 374https://doi.org/10.1098/rsta.2014.0301. 20140301.
- Melanson, A., Bell, T., Tarasov, L., 2013. Numerical modelling of subglacial erosion and sediment transport and its application to the North American ice sheets over the Last Glacial cycle. Ouat. Sci. Rev. 68, 154–174.
- Meyer, C.R., Downey, A.S., Rempel, A.W., 2018. Freeze-on limits bed strength beneath sliding glaciers. Nat. Commun. https://doi.org/10.1038/s41467-018-05716-1.
- Miller, K.G., Kominz, M.A., Browning, J.V., Wright, J.D., Mountain, G.S., Katz, M.E., Sugarman, P.J., Cramer, B.S., Christie-Blick, N., Pekar, S.F., 2005. The Phanerozoic record of global sea-level change. Science 310, 1293–1298.
- Mudelsee, M., Bickert, T., Lear, C.H., Lohmann, G., 2014. Cenozoic climate changes: a review based on time series analysis of marine benthic d18O records. Rev. Geophys. 52. https://doi.org/10.1002/2013RG000440.
- Naish, T., et al., 2009. Obliquity-paced Pliocene West Antarctic ice sheet oscillations. Nature 458, 322–328.
- Oerlemans, J., 1984. Numerical experiments on large-scale glacial erosion. Zeitschrift für Gletscherkunde und Glazialgeologie 20, 107–126.
- Pagani, M., Zachos, J.C., Freeman, K.H., Tipple, B., Bohaty, S., 2005. Marked decline in atmospheric carbon dioxide concentrations during the Paleogene. Science 309, 600–603
- Palike, H., Norris, R.D., Herrle, J.O., Wilson, P.A., Coxall, H.K., Lear, C.H., Shackleton, N.J., Tripati, A.K., Wade, B.S., 2006. The heartbeat of the Oligocene climate system. Science 314, 1894–1898.
- Paxman, G.J.G., Jamieson, S.S.R., Bentley, M.J., Ross, N., Watts, A.B., Leitchenkov, G., Armadillo, E., Young, D.A., 2019a. The role of lithospheric flexure in the landscape evolution of the wilkes subglacial basin and transantarctic mountains, East Antarctica. J. Geophys. Res.-Earth Surface 124, 812–829.
- Paxman, G.J.G., Jamieson, S.S.R., Hochmuth, K., Gohl, K., Bentley, M.J., Leitchenkov, G., Ferraccioli, F., 2019b. Reconstructions of antarctic topography since the eocene-oligocene boundary. Palaeogeogr. Palaeoclimatol. Palaeoecol. 535. https://doi.org/10. 1016/j.palaeo.2019.109346.
- Pollard, D., 2010. A retrospective look at coupled ice sheet-climate modeling. Clim.

- Change 100, 173-194.
- Pollard, D., DeConto, R.M., 2003. Antarctic ice and sediment flux in the Oligocene simulated by a climate-ice sheet-sediment model. Palaeogeogr. Palaeoclimatol. Palaeoecol. 198, 53–67.
- Pollard, D., DeConto, R.M., 2005. Hysteresis in Cenozoic Antarctic ice sheet variations. Glob. Planet. Chang. 45, 9–21.
- Pollard, D., DeConto, R.M., 2007. A coupled ice-sheet/ice-shelf/sediment model applied to a marine-margin flowline: forced and unforced variations. In: Hambrey, M.J., Christoffersen, P., Glasser, N., Hubbard, B. (Eds.), International Association of Sedimentologists Special Publication 39. Blackwell Publ., pp. 37–52 Glacial and Sedimentary Processes and Products.
- Pollard, D., DeConto, R.M., 2009. Modelling West Antarctic ice sheet growth and collapse through the past five million years. Nature 458, 329–332.
- Pollard, D., DeConto, R.M., 2012a. Description of a hybrid ice sheet-shelf model, and application to Antarctica. Geosci. Model Dev. 5, 1273–1295.
- Pollard, D., DeConto, R.M., 2012b. A simple inverse method for the distribution of basal sliding coefficients under ice sheets, applied to Antarctica. The Cryo 6, 953–971.
- Pollard, D., DeConto, R.M., Alley, R.B., 2015. Potential Antarctic Ice Sheet retreat driven by hydrofracturing and ice cliff failure. Earth Planet. Sci. Lett. 412, 112–121.
- Pollard, D., Chang, W., Haran, M., Applegate, P., DeConto, R., 2016. Large ensemble modeling of last deglacial retreat of the West Antarctic Ice Sheet: comparison of simple and advanced statistical techniques. Geosci. Model Dev. 9, 1697–1723.
- Rebesco, M., Larter, R.D., Camerlenghi, A., Barker, P.F., 1996. Giant sediment drifts on the continental rise west of the Antarctic Peninsula. Geo Mar. Lett. 16, 65–75.
- Schoof, C., 2007. Ice sheet grounding line dynamics: steady states, stability, and hysteresis. J. Geophys. Res. 112, F03S28. https://doi.org/10.1029/2006JF000664.
- Stagg, H.M.J., Colwel, J.B., Direen, N.G., O'Brien, P.E., Bernardel, G., Borissova, I., Brown, B.J., Ishirara, T., 2004. Geology of the continental margin of enderby and mac. Robertson lands, East Antarctica: insights from a regional data set. Mar. Geophys. Res. 25, 183–219.
- Stap, L.B., van de Wal, R.S.W., de Boer, B., Bintanja, R., Lourens, L.J., 2016. The MMCO-EOT conundrum: same benthic δ^{18} O, different CO₂. Paleoceanography 31, 1270–1282.
- Stap, L.B., van de Wal, R.S.W., de Boer, B., Bintanja, R., Lourens, L.J., 2017. The influence of ice sheets on temperature during the past 38 million years inferred from a onedimensional ice sheet-climate model. Clim. Past 13, 1243–1257.
- Sugden, D.E., Jamieson, S.S.R., 2018. The pre-glacial landscape of Antarctica. Scott. Geogr. J. https://doi.org/10.1080/14702541.2018.1535090.
- ten Brink, U.S., Schneider, C., 1995. Glacial morphology and depositional sequences of the Antarctic continental shelf. Geology 23, 580–584.
- ten Brink, U.S., Schneider, C., Johnson, A.H., 1995. Morphology and stratal geometry of the Antarctic continental shelf: insights from models. In: In: Cooper, A.K., Barker, P.F., Brancolini, G. (Eds.), Geology and Seismic Stratigraphy of the Antarctic Margin, vol. 68. American Geophysical Union, Washington D.C., pp. 1–24 Antarctic Research Series
- Uenzelmann-Neben, G., 2018. Variations in ice-sheet dynamics along the amundsen sea and bellingshausen sea West Antarctic ice sheet margin. Geol. Soc. Am. Bull. 131, 479–498. https://doi.org/10.1130/B31744.1.
- Uenzelmann-Neben, G., Gohl, K., 2012. Amundsen Sea sediment drifts: archives of modifications in oceanographic and climate conditions. Mar. Geol. 299–302, 51–62.
- van de Wal, R.S.W., de Boer, B., Lourens, L.J., Kohler, P., Bintanja, R., 2011.

 Reconstruction of a continuous high-resolution CO2 record over the past 20 million years. Clim. Past 7, 1459–1469.
- van den Berg, J., van de Wal, R.S.W., Oerlemans, J., 2006. Effects of spatial discretization in ice-sheet modelling using the shallow-ice approximation. J. Glaciol. 52, 89–98.
- Whittaker, J.M., Goncharov, A., Williams, S.E., Muller, R.D., Leitchenkov, G., 2013. Global sediment thickness data set updated for the Australian-Antarctic Southern Ocean. Geochem. Geophys. Geosyst. 14, 3297–3305.
- Wilson, D.S., Luyendyk, B.P., 2009. West Antarctic paleotopography estimated at the Eocene-Oligocene climate transition. Geophys. Res. Lett. 36, L16302. https://doi. org/10.1029/2009GL039297.
- Wilson, D.S., Jamieson, S.S.R., Barrett, P.J., Leitchenkov, G., Gohl, K., Larter, R.D., 2012. Antarctic topography at the Eocene-Oligocene boundary. Palaeogeogr. Palaeoclimatol. Palaeoecol. 335–336, 24–34.
- Wilson, D.S., Pollard, D., DeConto, R.M., Jamieson, S.S.R., Luyendyk, B.P., 2013. Initiation of the West antarctic ice sheet and estimates of total antarctic ice volume in the earliest Oligocene. Geophys. Res. Lett. 40, 4305–4309. https://doi.org/10.1029/ 2009GL039297.
- Wilson, G.S., Pekar, S.F., Naish, T.R., Passchier, S., DeConto, R.D., 2008. Chapter 9: the Oligocene-Miocene boundary - Antarctic climate response to orbital forcing. In: In: Florindo, F., Siegert, M. (Eds.), Developments in Earth and Environmental Sciences, vol. 8. pp. 369–400 Antarctic Climate Evolution.
- Wobbe, F., Lindeque, A., Gohl, K., 2014. Anomalous South Pacific lithosphere dynamic derived from new total sediment thickness estimates off the West Antarctic margin. Glob. Planet. Chang. 123, 139–149.
- Zhang, Y.G., Pagani, M., Liu, Z., Bohaty, S.M., DeConto, R., 2013. A 40-million-year history of atmospheric CO2. Phil. Trans. Roy. Soc. A 371, 20130096. https://doi.org/ 10.1098/rsta.2013.0096.